LETTER

doi:10.1038/nature23902

Alternative evolutionary histories in the sequence space of an ancient protein

Tyler N. Starr[1], Lora K. Picton[2] & Joseph W. Thornton[2,3]

To understand why molecular evolution turned out as it did, we must characterize not only the path that evolution followed across the space of possible molecular sequences but also the many alternative trajectories that could have been taken but were not. A large-scale comparison of real and possible histories would establish whether the outcome of evolution represents an optimal state driven by natural selection or the contingent product of historical chance events[1]; it would also reveal how the underlying distribution of functions across sequence space shaped historical evolution[2,3]. Here we combine ancestral protein reconstruction[4] with deep mutational scanning[5–10] to characterize alternative histories in the sequence space around an ancient transcription factor, which evolved a novel biological function through well-characterized mechanisms[11,12]. We find hundreds of alternative protein sequences that use diverse biochemical mechanisms to perform the derived function at least as well as the historical outcome. These alternatives all require prior permissive substitutions that do not enhance the derived function, but not all require the same permissive changes that occurred during history. We find that if evolution had begun from a different starting point within the network of sequences encoding the ancestral function, outcomes with different genetic and biochemical forms would probably have resulted; this contingency arises from the distribution of functional variants in sequence space and epistasis between residues. Our results illuminate the topology of the vast space of possibilities from which history sampled one path, highlighting how the outcome of evolution depends on a serial chain of compounding chance events.

We applied deep mutational scanning to the DNA-binding domain of a reconstructed ancestral steroid hormone receptor, whose historical trajectory of functional, genetic, and biochemical evolution is well understood. Steroid receptors are transcription factors that mediate the action of sex and adrenal steroids by binding to specific DNA sequences and regulating expression of target genes. The two major clades of receptors differ in their DNA specificity (Fig. 1a): oestrogen receptors prefer an inverted palindrome of AGGTCA (oestrogen response element, ERE)[13], whereas receptors for androgens, progestogens, and corticosteroids prefer AGAACA (steroid response element, SRE)[14]. Although some degeneracy is tolerated, these sequences represent the high-affinity consensus sites for each class[13,14] and have therefore been the focus of extensive biochemical characterization[15–18]. Previously, we reconstructed the ancestral protein from which all steroid receptors descend (AncSR1) and found that it specifically binds ERE[11,12]. After AncSR1 duplicated, one daughter protein diverged in function to yield AncSR2, which prefers SRE. Re-introducing three substitutions from this historical interval radically shifts the relative affinity of AncSR1 from ERE to SRE, and this effect is robust to uncertainty about the ancestral sequence[19]. These substitutions are located on the protein's recognition helix (RH), which directly contacts the response element's major groove[15–17]. Although they shift specificity, the RH substitutions alone reduce affinity below that required to activate transcription. Another eleven substitutions (11P) outside the RH that occurred during this evolutionary interval were permissive, increasing affinity for both ERE and SRE, allowing the protein to tolerate the function-switching RH substitutions[11].

To characterize alternative ways by which SRE specificity could have evolved (Fig. 1a), we focused on the RH, the only portion of the protein that directly contacts the nucleotides that vary between ERE and SRE. We prepared a library containing all 160,000 combinations of all 20 amino acids at four key sites in the RH: the three that historically shifted DNA specificity, plus a physically adjacent lysine that varies among the broader receptor superfamily (Fig. 1b). The library was constructed in AncSR1+11P, the genetic background that enabled the historical RH substitutions to alter DNA specificity. We engineered yeast reporter strains in which ERE or SRE drives expression of a fluorescent GFP reporter and showed that GFP activation directly relates to DNA affinity (Extended Data Fig. 1a)[18]. We transformed the library into each reporter and used fluorescence-activated cell sorting coupled to deep sequencing (FACS-seq) to quantify binding of each variant in the library to ERE or SRE (Extended Data Figs 1–3 and Extended Data Table 1). We classified genotypes as ERE-specific, SRE-specific, promiscuous, or inactive; results of all subsequent analyses were robust to the specific classification criteria (Extended Data Table 2).

We found 828 new RH variants that are SRE-specific, binding SRE as well or better than the historical outcome and displaying no activity on ERE (Fig. 1c). These alternative SRE-specific genotypes use amino acids with diverse biochemical characteristics (Fig. 1d), and they discriminate between SRE and ERE using different physical contacts (Fig. 1e, f and Extended Data Fig. 4). For example, the historical outcome (RH sequence GSKV) binds SRE in part by polar contacts from Lys28 to nucleotides A1 and G2, but the alternative outcome KAAI makes no polar contacts using residue 28, instead hydrogen bonding from Lys25 to A1, G2, and the opposite-strand nucleotide T-3 (Fig. 1e). It also exhibits novel mechanisms of ERE-exclusion: whereas GSKV leaves the hydrogen bonding potential of C-3 unsatisfied, KAAI also leaves G2 and T4 unpaired, because Ala28—unlike Lys28 of GSKV—cannot bond to G2, and Ile29 interferes with a hydrogen bond to T4 made by the conserved Arg33 residue (Fig. 1f and Extended Data Fig. 4c).

The historical outcome is therefore not unique in its genetic or biochemical mechanism of SRE specificity, but it might have been uniquely accessible from the ancestral RH. To investigate the distribution of functions across sequence space, we constructed a force-directed graph of functional RH variants (Fig. 2a). Each node represents a functional RH genotype, and edges connect nodes separated by one non-synonymous nucleotide mutation (steps). Although the vast majority of RH variants are non-functional, virtually all of the 1,351 functional variants are part of a single connected network that can be traversed without visiting non-functional genotypes[2]. The network contains clusters of densely interconnected variants that share distinguishing amino-acid states, with epistasis and the structure of the genetic code separating the clusters. ERE-specific, SRE-specific, and promiscuous

[1]Department of Biochemistry and Molecular Biology, University of Chicago, Chicago, Illinois 60637, USA. [2]Department of Ecology and Evolution, University of Chicago, Chicago, Illinois 60637, USA. [3]Department of Human Genetics, University of Chicago, Chicago, Illinois 60637, USA.

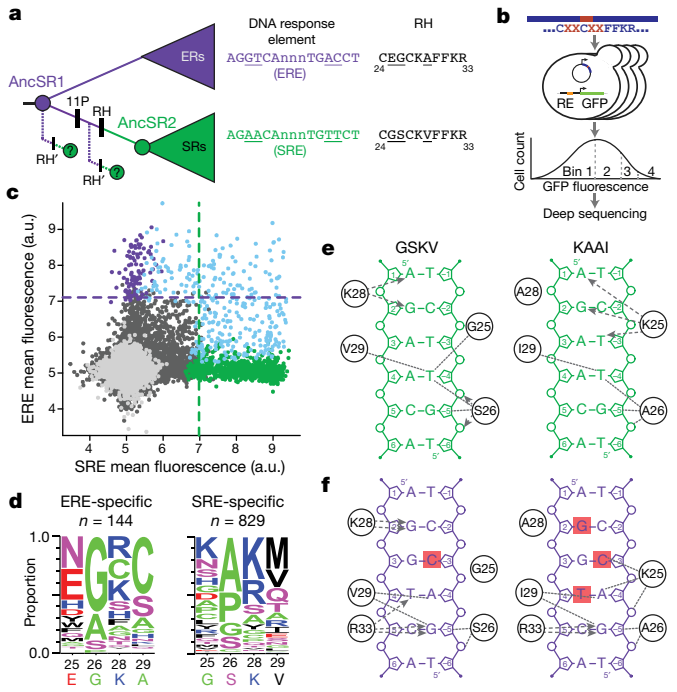

Figure 1 | Diverse sequences and mechanisms can yield the derived DNA specificity. a, The historical transition in DNA-binding specificity in steroid receptors occurred during a known phylogenetic interval and was caused by three changes in the protein's recognition helix (RH), which required permissive substitutions (11P)[11]. We searched for other RH mutations (RH′) that could have produced the derived function in the reconstructed ancestral background, before or after 11P. The DNA response element and protein RH sequence of each clade on the protein family phylogeny (residues 24–33) is shown; underlined, historically variable states. ERs, oestrogen receptors; SRs, other steroid receptors. Reconstructed ancestral proteins are coloured by their previously determined response element preference. **b**, FACS-seq assay for steroid receptor DNA recognition. Libraries of 160,000 RH variants were synthesized in the AncSR1 and AncSR1+11P backgrounds and cloned into yeast carrying an integrated ERE- or SRE-driven GFP reporter. Red Xs indicate variable residues in the RH. Each variant's activity was estimated by FACS-sorting cells transformed with the library, using deep sequencing to determine the distribution of each RH variant across fluorescence bins, and then estimating the mean fluorescence of cells carrying each variant. RE, response element. **c**, GFP activation on ERE and SRE by each variant in the AncSR1+11P background (a.u., arbitrary units). Purple dots, variants classified as ERE-specific; green, SRE-specific; blue, promiscuous; black, non-functional; grey, stop-codon variants. Purple line, activity of AncSR1:EGKA on ERE; green line, AncSR1+11P:GSKV on SRE. **d**, Frequency of residues at each variable position in ERE- and SRE-specific variants; *n*, number of variants in each class. Residues are coloured by biochemical category: red, acidic; blue, basic; magenta, polar uncharged; black, large non-polar; green, small non-polar. Residues and site numbers in AncSR1 and AncSR2 are shown. **e**, **f**, Diverse biochemical mechanisms for recognition of SRE (**e**) or ERE (**f**) by the historical derived RH (GSKV) and an alternative SRE-specific variant (KAAI). Contacts in structural models are shown between RH residues (circles) and DNA. Arrows, hydrogen bonds from donor to acceptor; dotted lines, non-bonded contacts. Red squares, bases that hydrogen bond in EGKA-ERE but are unsatisfied in these complexes. Only RH-DNA contacts that differ among complexes are shown (see Extended Data Fig. 4).

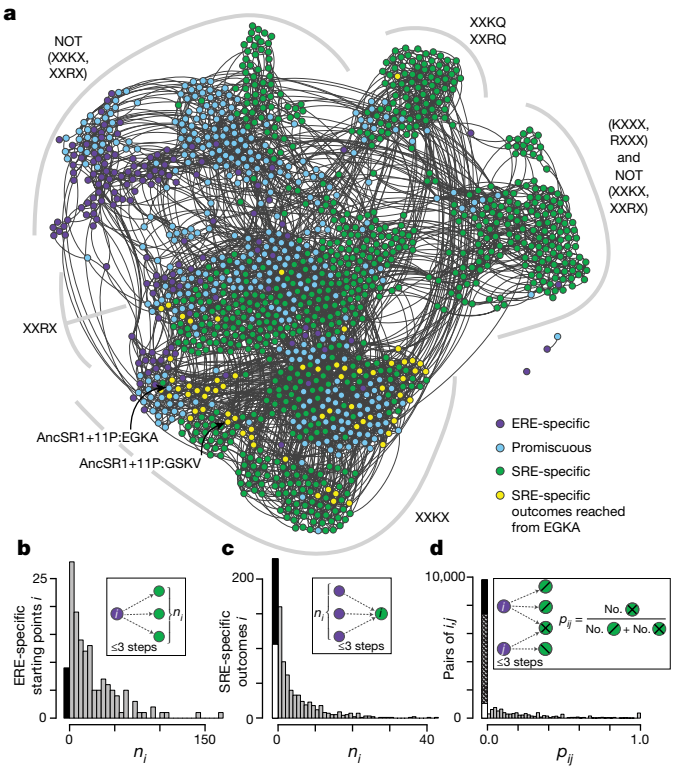

Figure 2 | Evolvability of SRE specificity in an ancestral sequence space. a, Force-directed graph shows the functional topology of the RH sequence space in the AncSR1+11P background. Nodes, all functional RH variants, coloured by specificity as in Fig. 1c; yellow, SRE-specific variants that are accessible from ancestral genotype EGKA in three or fewer mutational steps (the length of the historical trajectory). Edges, single non-synonymous nucleotide mutations. Clusters of densely connected nodes (grey arcs) are labelled by their defining genetic features; X, variable sites within a cluster. Historical ancestral and derived RH genotypes are indicated. **b**, Distribution of ERE-specific nodes (starting points) by number of SRE-specific nodes (outcomes) reached in three or fewer steps. Black, starting points that reach zero outcomes because epistasis results in non-functional intermediates[7,8]. **c**, Distribution of outcomes by number of starting points that reach it in three or fewer steps. Black, outcomes reached from zero starting points because of epistasis; white, because all starting points are more than three non-synonymous mutations away. **d**, Distribution of pairs of starting points by the fraction of outcomes within three or fewer steps that are shared. Black, pairs with zero shared outcomes because of epistasis; white, because starting points are too far apart to reach the same genotypes; hatched, because no mutually accessible genotypes are SRE-specific.

variants are interspersed throughout the network, resulting in a very large number of potential evolutionary paths among functions.

The ancestral and derived RHs (sequences EGKA and GSKV, respectively) are connected by a path of just 3 steps, whereas the most distant proteins in the functional network are 13 steps apart. From the ancestral starting point, GSKV is not uniquely accessible: 64 other SRE-specific RHs are accessible in 3 or fewer steps without passing through non-functional intermediates. Some of these alternative outcomes can be reached in just one or two steps, and these too exhibit biochemically diverse amino-acid states (Extended Data Fig. 5a). The accessibility of other SRE-specific outcomes persists when other evolutionary models are used. If selection against too-tight or too-weak binding allowed access only to genotypes with DNA affinity in a narrow range indistinguishable from the historical genotypes, there would still be hundreds of alternative SRE-specific outcomes, many of which would be easily accessible from the historical starting point (Extended Data Table 2, column E). Even when trajectories are allowed only if SRE affinity increases at every step—as would occur under positive selection for that function—there are numerous alternative SRE-specific genotypes with a non-trivial probability of evolving from the ancestral RH, and all of these are more likely than the historical outcome (Extended Data Fig. 5a–c). Taken together, these data indicate that the historical trajectory was not the only path, or even the shortest, from the ancestral RH to a derived protein that is SRE-specific.

Next, we asked whether the evolution of SRE specificity depended on the starting point within the large network of mutually accessible ERE-specific genotypes. All but two ERE-specific variants can access SRE specificity without passing through non-functional intermediates

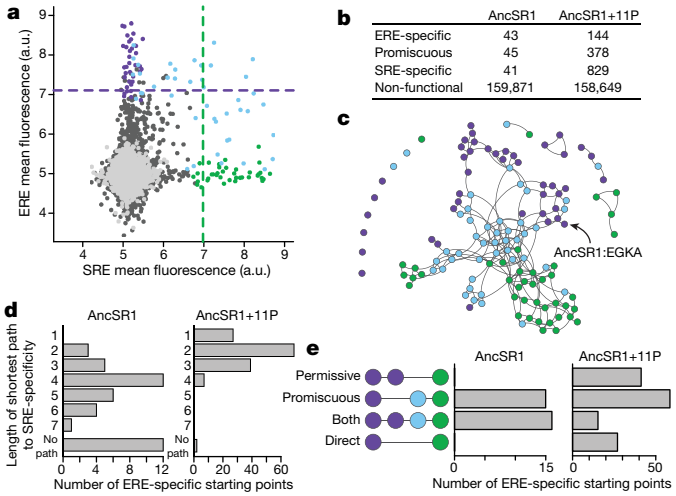

Figure 3 | Historical permissive substitutions enhanced evolvability of SRE specificity. a, GFP activation on ERE and SRE by each RH variant in the AncSR1 background; colours as in Fig. 1c. **b**, Number of variants in each functional class in the AncSR1 and AncSR1+11P backgrounds. **c**, Functional topology of the RH sequence space in AncSR1, represented as in Fig. 2a. **d**, Distribution of ERE-specific starting points by length of the shortest path to an SRE-specific outcome in AncSR1 (left) and AncSR1+11P (right). The 11P substitutions reduce the shortest path length ($P < 10^{-12}$, Wilcoxon rank-sum with continuity correction). **e**, 11P reduce the requirement for permissive and promiscuous intermediate steps. The shortest path to SRE specificity from each connected starting point in AncSR1 (left) or AncSR1 + 11P (right) was classified by trajectory type: permissive (via ERE-specific intermediates), promiscuous (via promiscuous intermediates), both, or direct (one-step path without permissive or promiscuous intermediates). Starting points with multiple equally short paths contribute proportionally to each category. Distributions differ between the networks ($P < 10^{-7}$, χ^2 test).

(Fig. 2a), and more than 90% can do so by paths no longer than the historical trajectory (Fig. 2b). Evolution of the derived specificity per se was therefore not strongly dependent on the starting point. Whether any particular SRE-specific genotype would evolve, however, could be contingent on where in the network of ERE-specific variants an evolutionary trajectory begins. For each SRE-specific RH, we therefore asked how many ERE-specific starting points could access it by a path no longer than the historical three-step trajectory (Fig. 2c). About one-third of possible SRE-specific genotypes are not easily reached from any possible starting point—some because the large diameter of the functional network means that the minimum genetic distance to the closest ERE-specific variant is more than three non-synonymous mutations, and some because epistasis requires trajectories longer than the minimum genetic distance to avoid nonfunctional intermediates[7,8]. Of the remaining SRE-specific variants, most (including the historical outcome GSKV) are readily accessible from just one or a few starting points, and even the most accessed outcome is easily reached from fewer than one-third of all possible starting points. As a result, most pairs of ERE-specific starting points reach entirely non-overlapping sets of SRE-specific outcomes (Fig. 2d), and these contain distinct sets of amino acids (Extended Data Fig. 6a). The evidence for dependence on starting point persists when path lengths longer than the historical trajectory are considered (Extended Data Fig. 6b–d) and when alternative evolutionary models are applied (Extended Data Table 2). Taken together, these data indicate that the derived specificity for SRE could have evolved in many ways from AncSR1+11P, but the underlying genetic and biochemical form depended strongly on the starting RH genotype that history happened to provide.

We next asked how the historical permissive substitutions affected the accessibility of the derived specificity and its dependence on starting point. We constructed and characterized the same four-site combinatorial RH library, this time in the AncSR1 background without 11P (Figs 1a and 3a and Extended Data Fig. 1). Removing 11P dramatically reduces the number of functional variants (Fig. 3b) and the connectivity of the network (Fig. 3c). Unlike the AncSR1+11P sequence space, many functional variants in AncSR1 are isolated and therefore cannot be reached from most other genotypes without passing through non-functional intermediates. Still, most functional RHs—including the ancestral RH (EGKA)—are interconnected in the primary subnetwork, where many SRE-specific RHs are accessible. Therefore, although the historically derived RH genotype GSKV requires the historical permissive substitutions, other genotypes with the derived specificity could have evolved without 11P. But trajectories in the AncSR1 sequence space are more complex. The shortest path from the ancestral RH to any SRE-specific variant is five steps long, compared to just one step in AncSR1 + 11P. Further, all paths require permissive RH steps that do not enhance SRE activity, and all paths require promiscuous intermediate genotypes (Extended Data Fig. 7a, b). Thus, without the historical permissive substitutions, other permissive mutations would have been required for SRE specificity to evolve from the ancestral genotype.

The 11P substitutions enhanced the accessibility of SRE specificity not only from the ancestral genotype but from all ERE-specific starting points. Whereas virtually all starting points in the AncSR1+11P network could access at least one SRE-specific node without passing through non-functional intermediates, over a quarter of ERE-specific variants in AncSR1 have no path to the derived specificity, and those that can access SRE specificity require longer paths (Fig. 3d). Removing the historical permissive substitutions also increases the proportion of ERE-specific starting points that require a permissive step before acquiring SRE activity (Fig. 3e). And, unlike the AncSR1+11P network, every path from ancestral to derived specificity in AncSR1 must pass through a promiscuous intermediate (Fig. 3e).

Finally, we investigated the mechanism by which the historical permissive substitutions enhanced the potential for evolution across the RH sequence space. The 11P substitutions were broadly permissive, increasing the number of SRE-specific genotypes in the network by a factor of 20 (Fig. 3b). Previous work suggests that increases in protein stability sometimes mediate generalized permissive effects[20–23], but 11P have been shown not to increase the stability of AncSR1 (ref. 11). We previously proposed that 11P permitted the historical RH substitutions by non-specifically increasing affinity for both response elements[11], which would explain the broadly permissive effect of 11P on many RH genotypes. This hypothesis makes four testable predictions, all of which are corroborated by our experiments. First, RH variants that do not depend on 11P to yield SRE specificity should have greater SRE affinity than those that require 11P, whether or not 11P are present; we compared the predicted affinity and FACS-seq mean fluorescence of all 11P-independent and 11P-dependent SRE-specific variants and found that this prediction holds true (Fig. 4a and Extended Data Fig. 8a–d). Second, 11P should not change the genetic determinants of binding within the RH; as predicted, the most enriched residues among SRE-specific variants do not change between the two networks, but 11P weakens the preference for some tolerated states over others (Fig. 4b and Extended Data Fig. 8e). Third, 11P should not change the biochemical mechanisms by which the RH confers specificity, a prediction we tested by identifying the biochemical properties at each RH site that predict specificity for ERE and SRE (Extended Data Fig. 8f); we found that the determinants of SRE specificity are not dramatically altered by 11P (Fig. 4c). Fourth, if 11P non-specifically enhance affinity by all RHs, they should add new functional genotypes across sequence space; we found that the set of variants permitted by 11P are not localized to some region of the network but instead surround the sparser set of variants that functioned independently of 11P (Fig. 4d, e). As a result, the non-specific effect of 11P on affinity enhanced the connectivity of the ancestral sequence

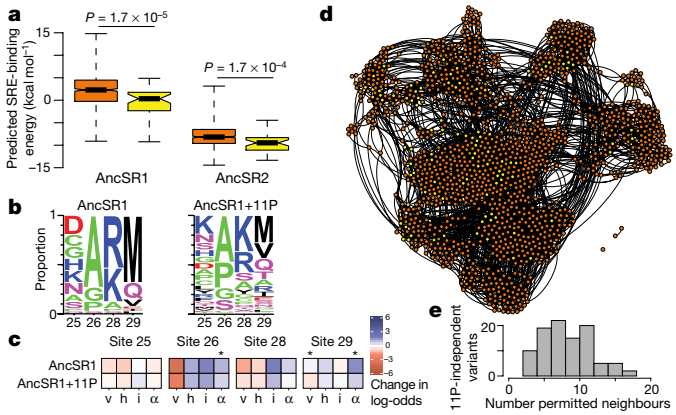

Figure 4 | Effect of historical permissive substitutions is mediated by non-specific increases in affinity. a, Predicted SRE-binding affinity of SRE-specific variants that require 11P (orange, $n = 790$) or do not (yellow, $n = 41$) in AncSR1 (left) or AncSR2 (right). In each category, the median (bar), 95% confidence interval (notch), interquartile range (box), and range (whiskers) are shown. *P* value, test for difference between medians (Wilcoxon rank-sum with continuity correction). **b**, Frequency of residues at variable RH sites among SRE-specific variants in AncSR1 (left) or AncSR1+11P (right). Residues are coloured by biochemical category as in Fig. 1d. **c**, Biochemical determinants of SRE specificity in AncSR1 (top) and AncSR1+11P (bottom). A multiple logistic regression model predicts the probability that each variant is SRE-specific from the properties of the residues at each variable site: v, volume; h, hydrophobicity; i, isoelectric point; α, α-helix propensity. Coloured boxes show best-fit coefficients of this model as the change in log-odds of being SRE-specific per unit change in each property. Asterisk, significant difference between AncSR1 and AncSR1+11P (*Z* test, $P < 0.05$). **d**, The AncSR1+11P RH functional network. Yellow, variants that are functional without 11P; orange, variants that require 11P. **e**, For each RH genotype that does not require 11P, the number of single-mutant neighbours that became functional when 11P was introduced.

network, increasing the number of paths from ERE to SRE specificity and reducing their length and complexity.

Our results shed light on the roles of determinism and chance in protein evolution[1,3,22,24]. The primary deterministic force is natural selection, which drives the evolution of forms that optimize fitness. Chance appears in two non-exclusive ways: as historical contingency, when the accessibility of some outcome depends on prior events that cannot be driven by selection for that outcome; and as stochasticity, when there are paths to numerous possible genotypes of similar function, and which one is realized is random (Extended Data Fig. 7c)[1]. Previous work has shown that historical function-switching substitutions in some proteins were contingent on prior permissive substitutions[11,20,25–27], but the overall roles of chance and determinism in the evolution of a new function can be understood only by characterizing other ways by which the function could have evolved. Our results point to strong stochasticity and contingency in the many histories by which SRE specificity could have evolved. Hundreds of genotypes encoding SRE specificity were accessible from AncSR1, but selection for that function alone could not have deterministically driven evolution down any of those paths, because all were contingent on permissive mutations—either the historical 11P or alternative permissive mutations within the RH. Which particular permissive mutations happened to occur determined which SRE-specific genotypes then became accessible. Further, given some permissive set of first steps, paths to numerous SRE-specific genotypes typically become available. Thus, evolution of any particular SRE-specific outcome—including the one that evolved during history—is contingent on the initial stochastic acquisition of some set of permissive mutations, followed by the subsequent stochastic realization of one of many possible ways to encode the derived function. These serial stochastic choices result in compounding contingency, magnifying the role of chance in evolution.

Some aspects of real and counterfactual history cannot be reconstructed, but our conclusions are likely to be robust to major forms of uncertainty. For example, the precise probability of any trajectory depends on population size and on the relationship between molecular function and fitness, but neither of these is known. Still, we found that contingency and stochasticity were important not only under scenarios emphasizing purifying selection and drift, but also under those favouring determinism, such as when selection drives continuous enhancement of the derived function or allows affinity within only a narrow range. Second, sequence space is so vast that we could explore only a limited portion. But contingency and stochasticity are likely to remain important when larger regions are considered. If these unexplored regions contain additional trajectories to SRE-specific outcomes, then the role of stochasticity in the choice among options would be even more important. Moreover, contingency on starting point arising from the distribution of SRE-specific genotypes across sequence space would persist even if new potential outcomes were discovered, and it would be magnified if those outcomes were even more distant than those we characterized. Finally, the dependence on permissive mutations that we observed would be eliminated only if there is a mutation at some other site that could somehow confer SRE activity on AncSR1 in a single step; this seems implausible, because all other residues are distant from the variable bases.

Despite the abundance of accessible SRE-specific genotypes near the ancestral and derived RHs (Extended Data Fig. 5d, e), the genotype that historically evolved is conserved among present-day descendants. It is possible that some unknown property made this sequence selectively superior to the many genotypes we found that are at least as effective at recognizing SRE and excluding ERE. But it could also be conserved because of factors that accumulated after it evolved. For example, a substitution can become epistatically entrenched by subsequent restrictive substitutions at other sequence sites[28,29]. A transcription factor's sequence may also become pleiotropically entrenched by subsequent mutations in the ensemble of response elements it binds[30]. If one of the many alternative SRE-specific outcomes had instead evolved from the ancestral protein by chance, it too could have been subsequently locked in, yielding conservation and the illusion that it evolved deterministically. The singularity of the present seems to rationalize the past. History leaves no trace of the many roads it did not take, or of the possibility that evolution turned out as it did for no good reason at all.

Online Content Methods, along with any additional Extended Data display items and Source Data, are available in the online version of the paper; references unique to these sections appear only in the online paper.

Received 23 March; accepted 8 August 2017.
Published online 13 September 2017.

1. Monod, J. *Chance and Necessity: An Essay on the Natural Philosophy of Biology* (Vintage Books, 1972).
2. Maynard Smith, J. Natural selection and the concept of a protein space. *Nature* **225,** 563–564 (1970).
3. Wagner, A. Neutralism and selectionism: a network-based reconciliation. *Nat. Rev. Genet.* **9,** 965–974 (2008).
4. Hochberg, G. K. A. & Thornton, J. W. Reconstructing ancient proteins to understand the causes of structure and function. *Annu. Rev. Biophys.* **46,** 247–269 (2017).
5. Fowler, D. M. *et al.* High-resolution mapping of protein sequence-function relationships. *Nat. Methods* **7,** 741–746 (2010).
6. Hietpas, R. T., Jensen, J. D. & Bolon, D. N. A. Experimental illumination of a fitness landscape. *Proc. Natl Acad. Sci. USA* **108,** 7896–7901 (2011).
7. Podgornaia, A. I. & Laub, M. T. Pervasive degeneracy and epistasis in a protein-protein interface. *Science* **347,** 673–677 (2015).
8. Wu, N. C., Dai, L., Olson, C. A., Lloyd-Smith, J. O. & Sun, R. Adaptation in protein fitness landscapes is facilitated by indirect paths. *eLife* **5,** e16965 (2016).
9. Aakre, C. D. *et al.* Evolving new protein-protein interaction specificity through promiscuous intermediates. *Cell* **163,** 594–606 (2015).
10. Sarkisyan, K. S. *et al.* Local fitness landscape of the green fluorescent protein. *Nature* **533,** 397–401 (2016).
11. McKeown, A. N. *et al.* Evolution of DNA specificity in a transcription factor family produced a new gene regulatory module. *Cell* **159,** 58–68 (2014).

12. Anderson, D. W., McKeown, A. N. & Thornton, J. W. Intermolecular epistasis shaped the function and evolution of an ancient transcription factor and its DNA binding sites. *eLife* **4,** e07864 (2015).
13. Carroll, J. S. *et al.* Genome-wide analysis of estrogen receptor binding sites. *Nat. Genet.* **38,** 1289–1297 (2006).
14. Watson, L. C. *et al.* The glucocorticoid receptor dimer interface allosterically transmits sequence-specific DNA signals. *Nat. Struct. Mol. Biol.* **20,** 876–883 (2013).
15. Luisi, B. F. *et al.* Crystallographic analysis of the interaction of the glucocorticoid receptor with DNA. *Nature* **352,** 497–505 (1991).
16. Schwabe, J. W., Chapman, L., Finch, J. T. & Rhodes, D. The crystal structure of the estrogen receptor DNA-binding domain bound to DNA: how receptors discriminate between their response elements. *Cell* **75,** 567–578 (1993).
17. Zilliacus, J., Carlstedt-Duke, J., Gustafsson, J. A. & Wright, A. P. Evolution of distinct DNA-binding specificities within the nuclear receptor family of transcription factors. *Proc. Natl Acad. Sci. USA* **91,** 4175–4179 (1994).
18. Bain, D. L. *et al.* Glucocorticoid receptor-DNA interactions: binding energetics are the primary determinant of sequence-specific transcriptional activity. *J. Mol. Biol.* **422,** 18–32 (2012).
19. Eick, G. N., Bridgham, J. T., Anderson, D. P., Harms, M. J. & Thornton, J. W. Robustness of reconstructed ancestral protein functions to statistical uncertainty. *Mol. Biol. Evol.* **34,** 247–261 (2017).
20. Bloom, J. D., Gong, L. I. & Baltimore, D. Permissive secondary mutations enable the evolution of influenza oseltamivir resistance. *Science* **328,** 1272–1275 (2010).
21. Gong, L. I., Suchard, M. A. & Bloom, J. D. Stability-mediated epistasis constrains the evolution of an influenza protein. *eLife* **2,** e00631 (2013).
22. Harms, M. J. & Thornton, J. W. Evolutionary biochemistry: revealing the historical and physical causes of protein properties. *Nat. Rev. Genet.* **14,** 559–571 (2013).
23. Starr, T. N. & Thornton, J. W. Epistasis in protein evolution. *Protein Sci.* **25,** 1204–1218 (2016).
24. Dickinson, B. C., Leconte, A. M., Allen, B., Esvelt, K. M. & Liu, D. R. Experimental interrogation of the path dependence and stochasticity of protein evolution using phage-assisted continuous evolution. *Proc. Natl Acad. Sci. USA* **110,** 9007–9012 (2013).
25. Ortlund, E. A., Bridgham, J. T., Redinbo, M. R. & Thornton, J. W. Crystal structure of an ancient protein: evolution by conformational epistasis. *Science* **317,** 1544–1548 (2007).
26. Harms, M. J. & Thornton, J. W. Historical contingency and its biophysical basis in glucocorticoid receptor evolution. *Nature* **512,** 203–207 (2014).
27. Natarajan, C. *et al.* Predictable convergence in hemoglobin function has unpredictable molecular underpinnings. *Science* **354,** 336–339 (2016).
28. Shah, P., McCandlish, D. M. & Plotkin, J. B. Contingency and entrenchment in protein evolution under purifying selection. *Proc. Natl Acad. Sci. USA* **112,** E3226–E3235 (2015).
29. Bridgham, J. T., Ortlund, E. A. & Thornton, J. W. An epistatic ratchet constrains the direction of glucocorticoid receptor evolution. *Nature* **461,** 515–519 (2009).
30. Lynch, M. & Hagner, K. Evolutionary meandering of intermolecular interactions along the drift barrier. *Proc. Natl Acad. Sci. USA* **112,** E30–E38 (2015).

Supplementary Information is available in the online version of the paper.

Acknowledgements We thank J. Bridgham and B. Metzger for technical advice, members of the Thornton laboratory past and present for comments, the University of Chicago's Flow Cytometry and Genomics Cores, and E. Thomas for poetic inspiration. This work was supported by National Institutes of Health R01GM104397 and R01GM121931 (J.W.T.), T32-GM007183 (T.N.S.), UL1-TR000430, and a National Science Foundation Graduate Research Fellowship (T.N.S.).

Author Contributions T.N.S. and J.W.T. conceived the project, designed experiments, and wrote the paper. L.K.P. and T.N.S. designed and constructed the reporter system. T.N.S. performed experiments and analysed data.

Author Information Reprints and permissions information is available at www.nature.com/reprints. The authors declare no competing financial interests. Readers are welcome to comment on the online version of the paper. Publisher's note: Springer Nature remains neutral with regard to jurisdictional claims in published maps and institutional affiliations. Correspondence and requests for materials should be addressed to J.W.T. (joet1@uchicago.edu).

Reviewer Information *Nature* thanks J. Bloom, A. de Visser, and D. Weinreich for their contribution to the peer review of this work.

METHODS

Construction and validation of a yeast assay for steroid receptor DNA-binding domain function. All work was performed in *Saccharomyces cerevisiae* strain K20 (CEN.PK 102-5B, *URA3*$^-$, *HIS3*$^-$, *LEU*$^-$)[31]. Oligonucleotide sequences used for cloning and sequencing are included in Supplementary Table 1. We constructed yeast reporter strains containing yeast enhanced GFP (yeGFP) under the control of a minimal *CYC1* promoter with two upstream ERE or SRE palindromes, integrated into the *ADE2* locus[31]. Colony PCR and Sanger sequencing confirmed correct integration of the *ERE$_2$–yeGFP* or *SRE$_2$–yeGFP* reporter. An additional 20 μg ml^{-1} adenine hemisulfate was added to all media to ameliorate *ADE2* disruption.

The yeast expression plasmid pTNS33 contains the AncSR1 DNA-binding domain (DBD, GenBank accession number AJC02122.1)[11] with an N-terminal SV40 nuclear localization sequence and Gal4 activation domain (AD) connected by a nine-residue linker (IQQGGSGGS). Expression of the AD-DBD fusion protein is controlled by the galactose-inducible *GAL1* promoter, in the background of the pRS413 plasmid[32] containing a *HIS* selection marker. We assembled pTNS33 by yeast homologous recombination using the LiAc/ssDNA/PEG method[33], selecting for growth on SC-His plates with 2% dextrose (+ D). We confirmed correct plasmid assembly by Sanger sequencing.

To validate the *ERE$_2$–yeGFP* and *SRE$_2$–yeGFP* reporters, a selection of previously assayed DBDs spanning a range of DNA-binding affinities[11,12] were cloned into the pTNS33 background and transformed into each yeast reporter strain. Individual colonies were inoculated in 3 ml SC-His with 2% raffinose (+ R), and incubated for 16 h at 30 °C and 225 r.p.m. in an orbital shaker incubator. Cells were back-diluted to 0.25 $A_{600\,nm}$ in SC-His with 2% galactose (+ G) to induce DBD expression and grown for an additional 24 h. Cells were pelleted and suspended to 1 $A_{600\,nm}$ in 1× TBS. We analysed 10,000 cells of each genotype by flow cytometry on a BD LSR-Fortessa 4-15, with 488 nm excitation and 530 nm emission. We used gates drawn empirically on forward-angle scattering/side-angle scattering (FSC/SSC) and forward-angle scattering height/forward-angle scattering area (FSC-H/FSC-A) plots (for example, Extended Data Fig. 2) to isolate a homogeneous cell population, from which we determined the mean per-cell green fluorescence. The relationship between mean GFP activation and previously measured binding affinities was fitted to a segmented-linear relationship in R[34] with the 'segmented' package[35].

Library generation. AncSR1 and AncSR1+11P RH libraries were constructed by synthesizing pools of oligonucleotides containing degenerate NNK codons at four variable sites in the RH and inserting these into coding sequences for the previously reconstructed AncSR1 DBD or the AncSR1+11P DBD, which contains the 11 previously identified historical permissive mutations[11]. These libraries encode all combinations of all 20 amino acids at the three RH sites that changed during the historical evolution of SRE specificity (sites 25, 26, and 29) and at the adjacent position (site 28), which physically interacts with the substituted residues[11] and varies among the broader nuclear receptor superfamily[36]. Each RH library contains 1,048,576 genetic variants, encoding 160,000 full-length proteins and 34,481 stop-codon-containing variants. To construct the libraries, 53-nucleotide single-stranded DNA oligonucleotides were synthesized (DNA2.0, Newark, California), containing variable RH sites and invariant flanking sequence identical to the respective plasmid sequences (Supplementary Table 1). Oligonucleotide pools were converted to double-stranded DNA by primer extension with Klenow polymerase and purified on a Qiagen MinElute column. Yeast expression plasmids containing AncSR1 or AncSR1+11P were modified by site-directed mutagenesis to introduce EcoRI and NcoI sites, which were cut to excise the native RH and linearize the vector to receive the oligonucleotide pool. Plasmid libraries were assembled via Gibson assembly, incubating 0.56 pmol gel-purified linear vector, 8.4 pmol oligonucleotide pool, and 120 μl 2× GA Master Mix (NEB) at 50 °C for 1 h. Assembled libraries were purified over DNA Clean & Concentrator columns (Zymo) and transformed into electrocompetent NEB5α *Escherichia coli* cells with a 2.5 kV electroporation pulse in 0.2 mm gap cuvettes. Aliquots of cells were serially diluted and plated on LB + carbenicillin to estimate transformation efficiencies. Remaining cells were grown overnight in LB + carbenicillin, and plasmids were harvested using a GenElute Midiprep plasmid purification kit. For both the AncSR1 and AncSR1+11P RH libraries, we obtained at least 20 times more transformants than the effective size of the library (Extended Data Table 1).

Each RH library (AncSR1 and AncSR1+11P) was independently transformed twice into each yeast reporter strain (ERE and SRE) for replicate FACS-seq analyses. We followed a yeast electroporation protocol[37], scaled up for ten times the number of cells and a total of 120 μg of library plasmid in 600 μl H_2O. An aliquot of cells was serially diluted and plated on SC-His + D to estimate transformation yield, which averaged 1.25 × 10^7 colony-forming units across the eight transformations (Extended Data Table 1). The remaining cells were grown to saturation in 500 ml SC-His + D. Consistent with previous observations[38], we observed that seven out of eight colonies post-transformation were multiple-vector transformants. We performed an additional passage, at which point multiple-vector clones were detected at fewer than one in eight colonies. A total of five passages occurred before quantification (see below), so at this rate of reduction multiple-vector transformants are expected to occur at a frequency no greater than 0.007 in the library. Furthermore, if many RH variants were false positives caused by co-transformation of non-functional with functional genotypes, then ones stop-codon-containing variants would have been classified as functional, but this was never observed. Passaged yeast library aliquots of 3 × 10^9 cells were flash frozen in liquid nitrogen and stored at −80 °C as 25% glycerol stocks.

Library induction and FACS. Yeast library aliquots were thawed on ice, added to 500 ml SC-His + D, and grown for 12 h at 30 °C and 225 r.p.m. Cells were diluted to 0.25 $A_{600\,nm}$ in 500 ml SC-His + R, and grown for an additional 12 h at 30 °C and 225 r.p.m. Cells were then diluted to 0.25 $A_{600\,nm}$ in 200 ml SC-His + G to induce DBD expression, and grown for 24 h at 30 °C and 225 r.p.m. Induced cells were spun at 3,000 *g* for 5 min, suspended to 3 × 10^7 cells per millilitre in 1× TBS, passed through a 40 μm nylon cell strainer, and stored on ice for sorting. Alongside each library induction, we induced isogenic controls expressing known DBDs according to the same protocol but at 3 ml volumes.

Each library was sorted into four bins on a BD FACSAria II. Initial gates were drawn to isolate homogenous cells and exclude doublets, using SSC/FSC and FSC-H/FSC-A scatterplots (Extended Data Fig. 2). We assigned sort gate boundaries to the AncSR1+11P/SRE library to correspond to the observed mean fluorescence of a stop-codon-containing variant, of AncSR1+11P:GSKV, and AncSR1+11P:GGKA, the variant with the highest previously known activation; these gates yielded four bins that captured 45%, 45%, 9.5%, and 0.5% of the library population, respectively. Gates for other libraries were assigned to yield the same bin sizes. To calibrate the arbitrary-unit fluorescence scales of sorting experiments conducted on different days, we transformed fluorescence values by a linear model fitted to the relationship between mean fluorescence of reference isogenic cultures induced and analysed in parallel to each library sorting experiment. Cells were sorted into SC-His + D with 34 μg ml^{-1} chloramphenicol to prevent bacterial contamination and stored on ice until ~10^8 cells were sorted. An aliquot of cells sorted into each bin was serially diluted and plated to estimate colony-forming unit recovery (Extended Data Table 1). Remaining cells were suspended to an estimated 200,000 cells per millilitre in SC-His + D + chloramphenicol, and grown for 16 h at 30 °C and 225 r.p.m. Plasmids were extracted from each outgrowth according to the protocol of ref. 39, which was scaled up 16-fold for bins 1 and 2, eightfold for bin 3, and threefold for bin 4 to avoid bottlenecks. Extracted plasmids were estimated to be present at a concentration of 2 × 10^6 plasmids per microlitre by comparing bacterial transformation efficiencies of yeast-extracted plasmid with pUC19 and bacterial-purified plasmid standards.

Sequencing and processing. We used PCR to amplify the variable RH region from post-sort plasmid aliquots; primers appended in-line barcodes[40] to identify the experiment and sort bin, along with binding sites for sequencing primers and Illumina flow cell adaptor sequences (Supplementary Table 1). Barcodes were of different lengths to stagger reads across clusters and were assigned to bins to optimize the distribution of base calls at each position during the initial rounds of sequencing. Multiple barcodes were used for bins 1 and 2, which contained the majority of cells. For each bin–barcode combination, PCR was conducted in eight replicate 50-μl aliquots, with 10 μl of plasmid template, 10 μl 5× HF buffer, 1 μl 10 mM dNTPs, 2.5 μl 10 μM forward and reverse primer, and 0.5 μl Phusion polymerase per reaction. PCRs were assembled on ice, transferred to a thermocycler block preheated to 98 °C, and subjected to 20 PCR cycles with 60 °C annealing. PCRs were gel-purified, quantified via BioAnalyzer and qPCR, and then pooled for sequencing according to the relative numbers of cells acquired in each bin. Single-end 50 bp reads spanning the barcode and RH sequence were acquired on an Illumina HiSeq2500.

We discarded sequence reads with an average Phred score <30 and sequences that did not perfectly match the barcode and invariant portion of the template. Reads were demultiplexed by barcode and further processed using tools from the FASTX-Toolkit (http://hannonlab.cshl.edu/fastx_toolkit/). RH variants with inconsistent read numbers between barcodes in the same bin were considered uncharacterized for that entire experiment. This procedure yielded filtered read counts in each sort bin greater than the number of cells sorted into that bin (Extended Data Table 1). To estimate the number of cells of a genotype that were sorted into a bin, we divided the number of sequence reads of a genotype in a bin by the average number of reads per cell in that bin.

Estimating mean fluorescence and standard error. We estimated the mean fluorescence of each variant in the library from the distribution of its reads across fluorescence sort bins using a maximum likelihood approach[41]. We first assessed the fit of various distributions to the observed per-cell fluorescence of a series of isogenic cultures of different RH genotypes analysed in isolation via flow cytometry, and found the logistic distribution to have the best fit by Akaike information criterion (Extended Data Fig. 1b, c). We then used the 'fitdistrplus' package[42] in R to

find the maximum likelihood mean fluorescence for each library variant given its distribution of cell counts across sort bins, the fluorescence boundaries of those bins, and the logistic distribution; this approach explicitly takes into account the fact that the fluorescence of a cell within a sort bin is not precisely measured and has been shown to be an unbiased approach for estimating underlying activities in FACS-seq analyses[41]. Estimates of mean fluorescence from the FACS-seq library characterization were compared between independent replicates (Extended Data Fig. 1d). Interval-censored per-cell observations from the two independent replicates were then pooled, and the maximum likelihood mean fluorescence for each variant estimated from these pooled data. These final estimates were compared with fluorescence observed directly for isogenic cultures of randomly selected clones from each library, which were isolated post-sort, genotyped, re-induced in isogenic cultures, and analysed via flow cytometry according to the protocol above (Extended Data Fig. 1e).

We estimated the standard error of mean fluorescence (s.e.m.) for genotypes on the basis of their depth of coverage (number of cells sampled) in two ways. First, we estimated s.e.m. from stop-codon-containing variants in each library by grouping them according to their depth of coverage and calculating the standard deviation of the sampling distribution of estimated mean fluorescence for variants in each group. Second, we leveraged variability in the mean fluorescence estimates from the two replicate FACS-seq experiments for each library: using coding variants for which the number of cells sampled between replicates is within 20% of each other, we calculated the difference between the estimate of mean fluorescence from the pooled data and the estimates from each of the two replicates, grouped variants by their average depth of coverage for the two replicates, and calculated the standard deviation of the distribution of differences for each group. Every variant in the library was then assigned the s.e.m. for the appropriate coverage depth group. These two approaches yielded a similar relationship between s.e.m. and sampling depth, but the second approach estimated higher s.e.m. at higher coverage depths (Extended Data Fig. 1g); to be conservative, we therefore used the second approach for further analyses.

Classifying strength of activation on each response element. We used mean fluorescence estimates to classify the strength with which each library variant bound to ERE and SRE using non-parametric comparisons with distributions of reference genotypes. A variant was classified as active on a response element if its mean fluorescence was significantly greater than that of stop-codon-containing variants contained in the library: for each variant, the *P* value for the null hypothesis that a variant was inactive was calculated as the proportion of stop-codon-containing variants of similar sampling depth with greater mean fluorescence than that of the variant of interest; variants were labelled 'active' if the null hypothesis could be rejected at a 5% false discovery rate (using the Benjamini–Hochberg procedure) or 'inactive' if the null hypothesis could not be rejected.

Each active variant was then subclassified as a weak or strong activator by comparing its mean fluorescence to that of the relevant ancestral genotypes (AncSR1:EGKA on ERE, or AncSR1+11P:GSKV on SRE). Specifically, for each active variant we performed a test of non-inferiority within an equivalence margin of 20% of the range between the average mean fluorescence of stop-codon-containing variants and the mean fluorescence of the ancestral reference. This test compares the mean fluorescence of a variant of interest with the fluorescence of cells with the relevant ancestral genotype, shifted to 80% of the range between the mean of stop-codon-containing variants and the ancestral reference. To determine whether a variant's fluorescence was greater than this shifted ancestral reference, we generated 10,000 bootstrap replicates from the shifted distribution of ancestral cellular fluorescence, with replicate size of similar sampling depth to the variant of interest; the mean fluorescence of each bootstrap replicate was calculated using the FACS gates and maximum likelihood procedure described above. The *P* value for the null hypothesis that a variant was a weak activator was calculated as the proportion of bootstrap replicates with fluorescence greater than that of the variant of interest; variants were classified as 'strong' if the null hypothesis could be rejected at a 5% false discovery rate (using the Benjamini–Hochberg procedure) or 'weak' if the null hypothesis could not be rejected. AncSR1:EGKA was represented by relatively few cells in the ERE library, resulting in an artificially low mean fluorescence determined by FACS-seq and a 'weak' classification, so it was manually classified as a strong activator on ERE by definition. For library classifications, we determined the reference activity of AncSR1:EGKA on ERE from an isogenic culture analysed in parallel to library sorts. Using the lower FACS-seq mean fluorescence measurement as the reference activity for this genotype did not alter our conclusions (Extended Data Table 2, column A).

Extrapolation to missing genotypes. Classification of variants that are rare in the library may not be reliable. We examined how agreement in classification between FACS-seq replicates is affected by sampling depth, and we found that the probability that a variant is classified as positive in one replicate if it is classified as positive in the other depends on sampling depth below 15 cells (Extended Data Fig. 1f). We therefore considered variants with 15 or fewer cells to be experimentally undetermined, accounting for 2.0–8.8% of all variants across the four DBD/response element combinations (Extended Data Table 1). To predict the classification of these variants, we used a continuation ratio ordinal logistic regression model that predicted the probability that a variant was strong, weak, or inactive from its genotype, trained on the empirical classification of all the determined genotypes in the library. We modelled amino-acid states as potentially contributing first-order main effects (20 states × 4 positions = 80 parameters) and pairwise epistatic effects ($_4C_2 \times 20^2 = 2{,}400$ parameters). We fitted these models to the observed classifications in each library using a coordinate-descent fitting algorithm with L_1 penalization, as implemented in the 'glmnetcr' package[43] in R. We used tenfold cross-validation to determine the quality of model predictions and to select the penalization parameter λ. We set $\lambda = 10^{-5}$ to obtain a high true positive rate without compromising the positive predictive value (Extended Data Fig. 3).

Classifying response element specificity. The specificity of each variant was determined from its functional classification on ERE and SRE. ERE-specific variants are strong on ERE and inactive on SRE; SRE-specific variants are strong on SRE and inactive on ERE; promiscuous variants are strong on one response element and strong or weak on the other; and non-functional variants are not strong on either response element. The false positive rate was very low, with no stop-codon-containing variants classified as functional. AncSR1+11P:EGKA is classified as promiscuous, because it has very strong ERE activity and SRE activity that is very weak but statistically distinguishable from background, consistent with previous observations[11].

A small number of RH variants were unexpectedly inferred to be functional in AncSR1 but non-functional in AncSR1+11P (Extended Data Fig. 8a–c). To validate this observation, we re-cloned the three SRE-specific variants with the largest reduction in fluorescence when 11P were included (CARV, HARV, HPRM) and assessed their SRE activation in the AncSR1 and AncSR1+11P backgrounds in isogenic cultures by flow cytometry; for comparison, we also validated a putatively 11P-independent genotype (KASM) and two 11P-dependent variants (SPKM, YGKQ), alongside GSKV for reference. Inductions were conducted in triplicate, each from an independent transformant. Classifications of the three comparison genotypes were all confirmed; however, the three genotypes that were putatively restricted by 11P showed no reduction in fluorescence in this assay, indicating that they were falsely classified as non-functional in the AncSR1+11P FACS-seq assay (Extended Data Fig. 8c). Notably, the predictive logistic regression correctly predicts that these three variants are strong SRE-binders in the AncSR1+11P background. These three variants manifested strong growth defects in the AncSR1+11P background, even in the ERE strain in which they do not activate GFP expression.

Robustness of results to classification method. We tested the robustness of our conclusions to alternative methods for classifying variants as functional. These included the following: (A) using the internal library AncSR1:EGKA mean fluorescence estimated by FACS-seq as the reference level of AncSR1 activation on ERE; (B) increasing the margin of equivalence to 50% of the activity difference between ancestral and stop-codon-containing variants; (C) classifying any active variant (weak or strong) as functional; (D) using the 80% mark of the range from stop-codon-containing to ancestral variants as a hard threshold rather than a null hypothesis for statistical testing; (E) defining functional variants as between 80% and 120% of the ancestral activity, so that extremely strong binders were classified as non-functional; (F) using predicted classifications for all variants, with experimental classifications used only to train predictive models; (G) using no predicted classifications, and labelling all undetermined genotypes as non-functional; (H) using for each variant the strongest functional class as predicted or determined by experiment; (I) using the experimental classification for a variant only if it was identical between replicates and predicting all others; and (J) using the per-variant estimates of the s.e.m. on the basis of coverage depth to calculate a *P* value that a variant was inactive or weakly active given a normal distribution, rejecting each null hypothesis at a 5% false discovery rate as above. When appropriate, ordinal logistic regression models were re-trained to predict missing genotypes under each scheme. These alterations made no qualitative differences to our conclusions (Extended Data Table 2).

Network construction and trajectories through sequence space. Network representations of functional RH variants in the AncSR1 and AncSR1+11P backgrounds were constructed using the R package 'rgexf'[44] and the network visualization program Gephi[45]. Nodes representing RH variants were connected by edges if any genetic encoding of their protein-coding sequences could be interconverted with a single-nucleotide mutation given the standard genetic code. The network was represented as a force-directed graph, which clusters nodes in two-dimensional space on the basis of connectivity: nodes tend to repel each other, but each edge between connected nodes provides an attractive force; in the 'equilibrium' layout, sets of densely interconnected nodes tend to cluster to the

exclusion of less connected nodes. Force-directed graph layouts were constructed with the ForceAtlas2 method in LinLog mode, Gravity 1.0, and Scaling 0.8 (AncSR1) or 0.125 (AncSR1+11P).

We used the 'igraph' package[46] in R to characterize the set of paths between functional nodes. A step was defined as a non-synonymous nucleotide mutation between two functional variants; synonymous mutations within a single node were not considered as contributing to trajectory length. The graph was directed, so that trajectories could proceed from ERE to SRE specificity directly or via a promiscuous intermediate; non-functional intermediates[2] and functional reversions were not allowed, but 'neutral' steps within a functional class were allowed. Epistasis was inferred when the shortest path between two nodes was longer than the minimum genetic distance between genotypes[7,8]; epistasis could arise because the state at one site specifically modulated the functional effect of some state at another site or because of nonlinearity in the genotype–phenotype map[47], such as the threshold we used to classify variants as functional.

The distributions of shortest path length to SRE specificity from ERE-specific starting points in the AncSR1 and AncSR1+11P networks were compared using a Wilcoxon rank-sum test with continuity correction, as observations were not normally distributed. The number of ERE-specific starting points in each network that required permissive steps and/or promiscuous intermediates on their shortest path to SRE specificity was compared via a χ^2 test. All categories had an expected value of 5 or greater.

To compare genotypic states among outcomes reached from different ERE-specific starting points, we calculated the frequency distribution of amino-acid states at each sequence site for the set of outcomes reached from each starting point; we then calculated the Jensen–Shannon (J–S) distance between these distributions for pairs of starting points. To capture a true amino-acid state distribution across outcomes, we only considered ERE-specific starting points that accessed at least 15 outcomes (the median across all ERE-specific starting points). We compared these observed J–S distances with a null expectation of J–S distances in the absence of structure in sequence space, in which we randomly sampled two sets of variants from all possible SRE-specific outcomes according to the same sample sizes used in each real comparison, and calculated the J–S distance between these randomly sampled distributions.

We also considered a regime in which SRE-binding affinity is under strong selection, such that SRE-binding affinity is required to increase with each step; such a scenario has a strong potential to make evolution deterministically favour a single outcome. In this scheme, a step from one genotype to a neighbour was allowed only if the lower bound of the 90% confidence interval of the neighbour's mean SRE fluorescence, estimated from its mean and s.e.m., was greater than the upper bound of the confidence interval of the starting genotype (indicating $P < 0.02$, ref. 48). We then calculated the probability of each accessible trajectory using two previously described models[8]: in the equal fixation model, any step that enhances SRE affinity from a particular node is equally likely to occur; in the correlated fixation model, the probability that an SRE-affinity-enhancing step occurs is directly proportional to the degree to which it increases SRE mean fluorescence, relative to the other SRE-enhancing steps available from the given node.

Structural modelling and predictions of RE-binding affinity. We used FoldX[49] to predict the affinity to SRE of all RH variants that were 11P-dependent (SRE-specific in the AncSR1+11P background and non-functional in AncSR1), or 11P-independent (SRE-specific in AncSR1; Extended Data Fig. 8a). For structure-based affinity prediction, we used the crystal structures of the AncSR1 DBD bound to ERE (Protein Data Bank (PDB) accession number 4OLN) and the AncSR2 DBD bound to SRE (PDB 4OOR) as starting points, with crystallographic waters and non-zinc ions removed. We removed chains E, F, K, and L from the 4OOR structure. We used the RepairPDB function to optimize both DBD structures according to the FoldX force field, and we used the BuildModel function to mutate the AncSR1/ERE structure to AncSR1:GSKV/SRE. The BuildModel function was then used to model each SRE-specific RH variant in complex with SRE on each of the AncSR1 and AncSR2 DBD structures, and the AnalyzeComplex function was used to predict the total DNA-binding energy of each protein variant with SRE. The predicted binding energies of 11P-dependent and 11P-independent variants were compared using a non-parametric Wilcoxon rank-sum test with continuity correction, as data were not normally distributed. This test was conducted independently for energies predicted using the AncSR1 and AncSR2 structures. To compare these same groups as directly estimated in FACS-seq, a Wilcoxon rank-sum test with continuity correction was used, as data were not normally distributed.

To characterize the diversity in biochemical mechanisms of SRE specificity, we analysed FoldX models of the ten most active SRE-specific variants that were identified in our AncSR1+11P FACS-seq experiment. We modelled binding to SRE using the AncSR2/SRE structure as described above and binding to ERE using the crystal structure of the AncSR2:EGKA DBD bound to ERE (PDB 4OND), with water and non-zinc ions removed and optimized using the RepairPDB function. To illustrate protein–DNA contacts made in each structural model, we used NUCPLOT[50] to identify all hydrogen bonds with distances $\leq$3.35Å between non-hydrogen atoms and non-bonded packing contacts $\leq$3.90Å. Summary figures display the union of contacts made by a residue in either of the half sites of the response element palindrome; we only illustrate residues whose contacts vary among the analysed structures.

To ensure structural inferences converge, we built each SRE- and ERE-bound FoldX model a second time. We observed convergence in all polar contacts (and absence thereof in ERE structures) illustrated in Fig. 1 and Extended Data Fig. 4. Only several non-bonded contacts were not replicated: I29/T–4 in KAAI/SRE; Q29/A4 and Q29/T–4 in YGKQ/SRE; M29/T–3 in KSAM/SRE; and K25/G2 and K25/T–3 in KASM/SRE. To determine whether electrostatic clashes in ERE-bound structures could be satisfied by bridged water molecules[51], models were built again using the BuildModel function with predicted waters. In some cases (GGRT, YGKQ, DSKM, CGRV), but not all (GSKV, KAAI, PAKE, KSAM, DPKQ, SAKE, KASM), polar groups on ERE that were not satisfied by direct interaction with protein side chains are predicted to be satisfied by water bridges between protein and DNA.

Biochemical determinants of response-element-binding specificity. Logos illustrating the frequency with which each amino-acid state is found at each position among variants of a functional class were constructed using WebLogo[52]. Since our sequence space is combinatorially complete (all 160,000 genotypes are classified, either by FACS-seq or via prediction), the logo plots do not need to be normalized by background input frequencies. To evaluate similarity of the frequency profiles between classes of variants, the frequency of each amino-acid state in a class was centred log-ratio transformed, the appropriate transformation before computing correlations among compositional data; a pseudocount of one was added to the number of observations of each amino acid to allow log-transformation of states observed zero times. The Spearman rank correlation coefficient was computed for the correlation between functional classes.

To identify the biochemical properties of amino acids that contribute to DNA specificity, we developed a multiple logistic regression model that describes the probability that an RH variant specifically binds a response element as a function of the biochemical properties of the amino-acid states at each of its four variable RH positions. The model includes four properties (hydrophobicity, volume, isoelectric point, and α-helix propensity), with the values for each amino acid's properties from ref. 53, which we then centred and standardized; the effect of a unit change in each property at each site on the log-odds of being a specific binder is reflected in a model coefficient, which together make up the model's free parameters. We used R to find the values of these coefficients that best fitted the observed classifications for each DBD/RE combination. Differences in the contribution of a property to specificity were identified if its associated coefficients in two models differed by a Z test ($P < 0.05$ with no correction for multiple testing)[54].

Data and code availability. Raw sequencing data have been deposited in the NCBI Sequence Read Archive under BioProject number PRJNA362734. Processed data and scripts to reproduce analyses are available at github.com/JoeThorntonLab/nature-2017_RH-scanning. A list of all RH sequences and their specificity classifications as used in the text is available in Supplementary Table 2. All other data are available from the corresponding author upon reasonable request.

31. Fox, J. E., Bridgham, J. T., Bovee, T. F. H. & Thornton, J. W. An evolvable oestrogen receptor activity sensor: development of a modular system for integrating multiple genes into the yeast genome. *Yeast* **24,** 379–390 (2007).
32. Mumberg, D., Müller, R. & Funk, M. Yeast vectors for the controlled expression of heterologous proteins in different genetic backgrounds. *Gene* **156,** 119–122 (1995).
33. Gietz, R. D. & Woods, R. A. Transformation of yeast by lithium acetate/single-stranded carrier DNA/polyethylene glycol method. *Methods Enzymol.* **350,** 87–96 (2002).
34. R Core Team. R: A language and environment for statistical computing (R Foundation for Statistical Computing, 2016).
35. Muggeo, V. M. R. segmented: an R package to fit regression models with broken-line relationships. *R News* **8,** 20–25 (2008).
36. Sluder, A. E., Mathews, S. W., Hough, D., Yin, V. P. & Maina, C. V. The nuclear receptor superfamily has undergone extensive proliferation and diversification in nematodes. *Genome Res.* **9,** 103–120 (1999).
37. Benatuil, L., Perez, J. M., Belk, J. & Hsieh, C. M. An improved yeast transformation method for the generation of very large human antibody libraries. *Protein Eng. Des. Sel.* **23,** 155–159 (2010).
38. Scanlon, T. C., Gray, E. C. & Griswold, K. E. Quantifying and resolving multiple vector transformants in *S. cerevisiae* plasmid libraries. *BMC Biotechnol.* **9,** 95 (2009).
39. Fowler, D. M., Stephany, J. J. & Fields, S. Measuring the activity of protein variants on a large scale using deep mutational scanning. *Nat. Protocols* **9,** 2267–2284 (2014).
40. Mir, K., Neuhaus, K., Bossert, M. & Schober, S. Short barcodes for next generation sequencing. *PLoS ONE* **8,** e82933 (2013).

41. Peterman, N. & Levine, E. Sort-seq under the hood: implications of design choices on large-scale characterization of sequence-function relations. *BMC Genomics* **17,** 206 (2016).
42. Delignette-Muller, M. L. & Dutang, C. fitdistrplus: an R package for fitting distributions. *J. Stat. Softw.* **64,** http://dx.doi.org/10.18637/jss.v064.i04 (2015).
43. Archer, K. J. & Williams, A. A. A. L1 penalized continuation ratio models for ordinal response prediction using high-dimensional datasets. *Stat. Med.* **31,** 1464–1474 (2012).
44. Vega Yon, J., Fábrega Lacoa, J. & Kunst, J. B. rgexf: build, import and export GEXF graph files. R package version 0.15.3. https://CRAN.R-project.org/package=rgexf (2015).
45. Bastian, M., Heymann, S. & Jacomy, M. Gephi: an open source software for exploring and manipulating networks. In *Int. AAAI Conference on Weblogs and Social Media,* vol. 8, 361–362 (Association for the Advancement of Artificial Intelligence, 2009).
46. Csardi, G. & Nepusz, T. The igraph software package for complex network research. *InterJ. Complex Syst.* **1695,** 1–9 (2006).
47. Sailer, Z. R. & Harms, M. J. Detecting high-order epistasis in nonlinear genotype-phenotype maps. *Genetics* **205,** 1079–1088 (2017).
48. Knol, M. J., Pestman, W. R. & Grobbee, D. E. The (mis)use of overlap of confidence intervals to assess effect modification. *Eur. J. Epidemiol.* **26,** 253–254 (2011).
49. Schymkowitz, J. *et al.* The FoldX web server: an online force field. *Nucleic Acids Res.* **33,** W382–W388 (2005).
50. Luscombe, N. M., Laskowski, R. A. & Thornton, J. M. NUCPLOT: a program to generate schematic diagrams of protein-nucleic acid interactions. *Nucleic Acids Res.* **25,** 4940–4945 (1997).
51. Schymkowitz, J. W. H. *et al.* Prediction of water and metal binding sites and their affinities by using the Fold-X force field. *Proc. Natl Acad. Sci. USA* **102,** 10147–10152 (2005).
52. Crooks, G. E., Hon, G., Chandonia, J.-M. & Brenner, S. E. WebLogo: a sequence logo generator. *Genome Res.* **14,** 1188–1190 (2004).
53. Abriata, L. A., Palzkill, T. & Dal Peraro, M. How structural and physicochemical determinants shape sequence constraints in a functional enzyme. *PLoS ONE* **10,** e0118684 (2015).
54. Paternoster, R., Brame, R., Mazerolle, P. & Piquero, A. Using the correct statistical test for the equality of regression coefficients. *Criminology* **36,** 859–866 (1998).

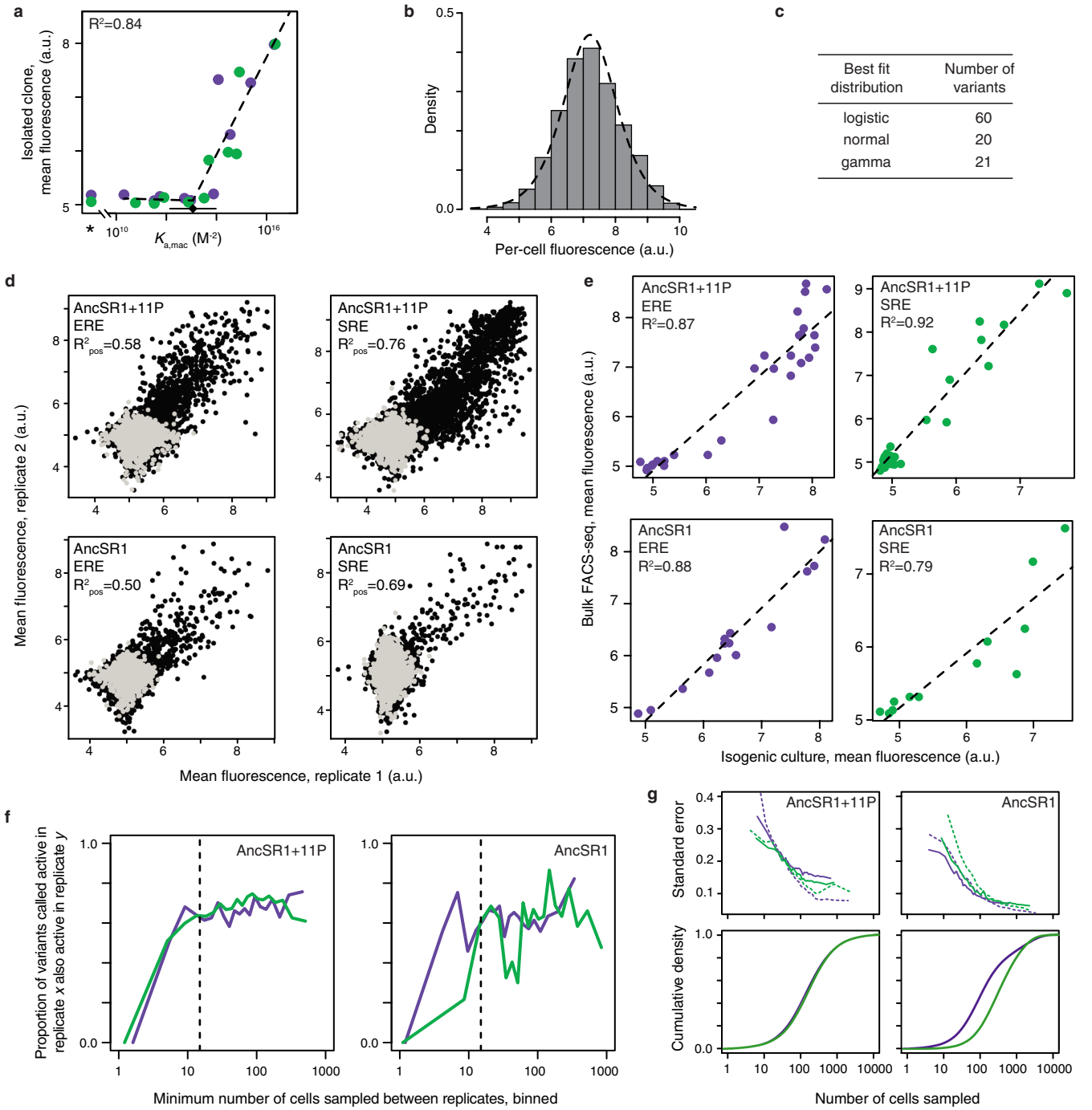

Extended Data Figure 1 | Design and validation of a yeast FACS-seq assay for steroid receptor DNA-binding function. a, GFP activation in ERE (purple) and SRE (green) yeast reporters correlates with previously measured protein–DNA binding affinity[11,12]. Asterisk, stop-codon-containing variant. Dashed line, best fit segmented-linear relationship between GFP activation and $\log_{10}(K_{a,mac})$ **b**, Histogram of the per-cell green fluorescence for AncSR1 on ERE measured via flow cytometry, fitted to a logistic distribution (dashed line). **c**, Distributions providing the best fit to flow cytometry data for isogenic cultures of 101 DBD variants, using Akaike information criterion. **d**, Comparisons of mean fluorescence estimates between FACS-seq replicates of each protein/response element combination. Black points, coding RH variants; light grey, stop-codon-containing variants. R^2_{pos}, squared Pearson correlation coefficient for variants with mean fluorescence significantly higher than stop-codon-containing variants in either or both replicates. **e**, Comparisons between mean fluorescence as determined in FACS-seq and via flow cytometry analysis of isogenic cultures for a random selection of clones from each library. Dashed line, best-fit linear regression. **f**, Robustness of classification to sampling depth. Variants were binned according to the minimum number of cells with which they were sampled in either replicate. Below 15 cells sampled (dashed line), the probability that a variant called active in one replicate was also called active in the other is dependent on sampling depth; to minimize errors due to sampling depth, we eliminated as 'undetermined' all variants with fewer than 15 cells sampled after pooling replicates. **g**, Standard error of mean fluorescence estimates (s.e.m.) in each library as a function of sampling depth. Top: for each background, the relationship between s.e.m. and sampling depth for ERE (purple) and SRE (green) libraries, as estimated from the sampling distribution of stop-codon-containing variants (dotted lines) or variability in mean fluorescence estimates between replicates (solid lines). Bottom: the cumulative fraction of coding variants in each library having a certain number of cells sampled in the pooled data.

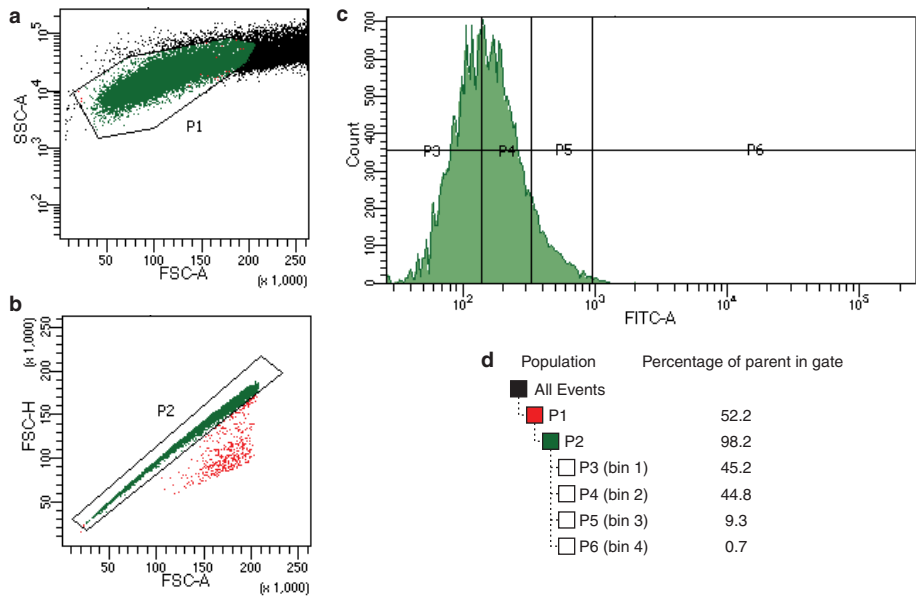

Extended Data Figure 2 | Representative FACS gates for library sorting. **a**, A scatterplot of side-angle scattering (SSC-A) and forward-angle scattering (FSC-A) selects for a homogenous cell population (P1). **b**, A scatterplot of the height of the per-cell forward scatter peak (FSC-H) and the integrated area of this peak (FSC-A) excludes events where multiple cells pass through the detector simultaneously (P2). **c**, Final sort bins (P3–P6) are drawn on the distribution of green fluorescence (FITC-A). **d**, Table showing the hierarchical parentage of sort gates and the percentage of events that fall in each bin.

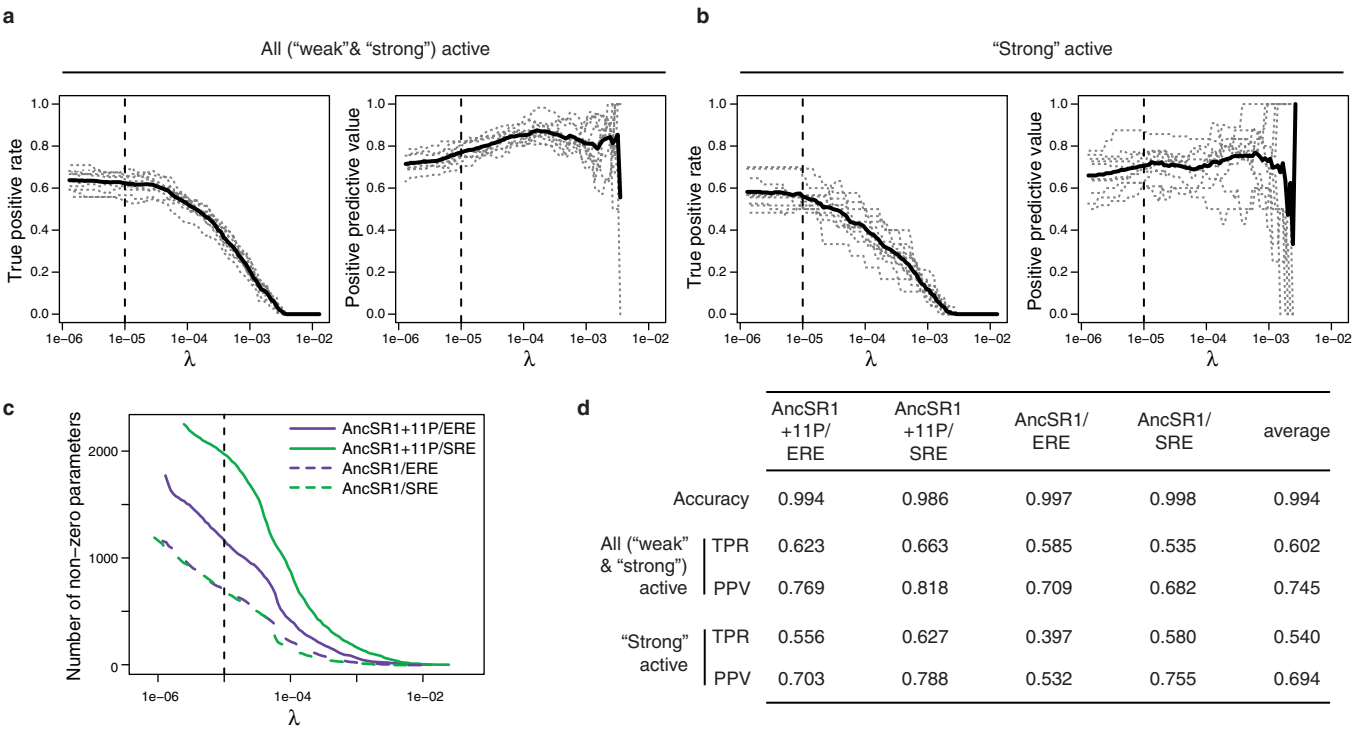

d

		AncSR1 +11P/ ERE	AncSR1 +11P/ SRE	AncSR1/ ERE	AncSR1/ SRE	average
Accuracy		0.994	0.986	0.997	0.998	0.994
All ("weak" & "strong") active	TPR	0.623	0.663	0.585	0.535	0.602
	PPV	0.769	0.818	0.709	0.682	0.745
"Strong" active	TPR	0.556	0.627	0.397	0.580	0.540
	PPV	0.703	0.788	0.532	0.755	0.694

Extended Data Figure 3 | Models to predict the function of missing genotypes. For each protein/response element combination, a continuation ratio ordinal logistic regression model was constructed to predict the functional class of a variant as a function of its four RH amino-acid states, including possible first-order main effects and second-order pairwise epistatic effects. Tenfold cross-validation was used to select the penalization parameter λ and evaluate performance. **a**, **b**, True positive rate (left, TPR, the proportion of experimental positives that are predicted positive) and positive predictive value (right, PPV, the proportion of predicted positives that are experimentally positive) are shown as a function of λ for AncSR1+11P on ERE. Classifications were evaluated for (**a**) all active (weak and strong) versus inactive variants and (**b**) strong active versus weak active and inactive variants. Grey dotted lines, cross-validation replicates; solid line, mean. Dashed line shows the chosen value of $\lambda = 10^{-5}$; as λ continues to decrease beyond $\lambda = 10^{-5}$, the true positive rate plateaus but positive predictive value continues to decline. **c**, The number of non-zero parameters included in each model as a function of λ. Dashed line, $\lambda = 10^{-5}$. **d**, Summary of performance metrics from tenfold cross-validation for each model with $\lambda = 10^{-5}$. Accuracy is the proportion of predicted classifications (strong, weak, and inactive) that match their experimentally determined classes.

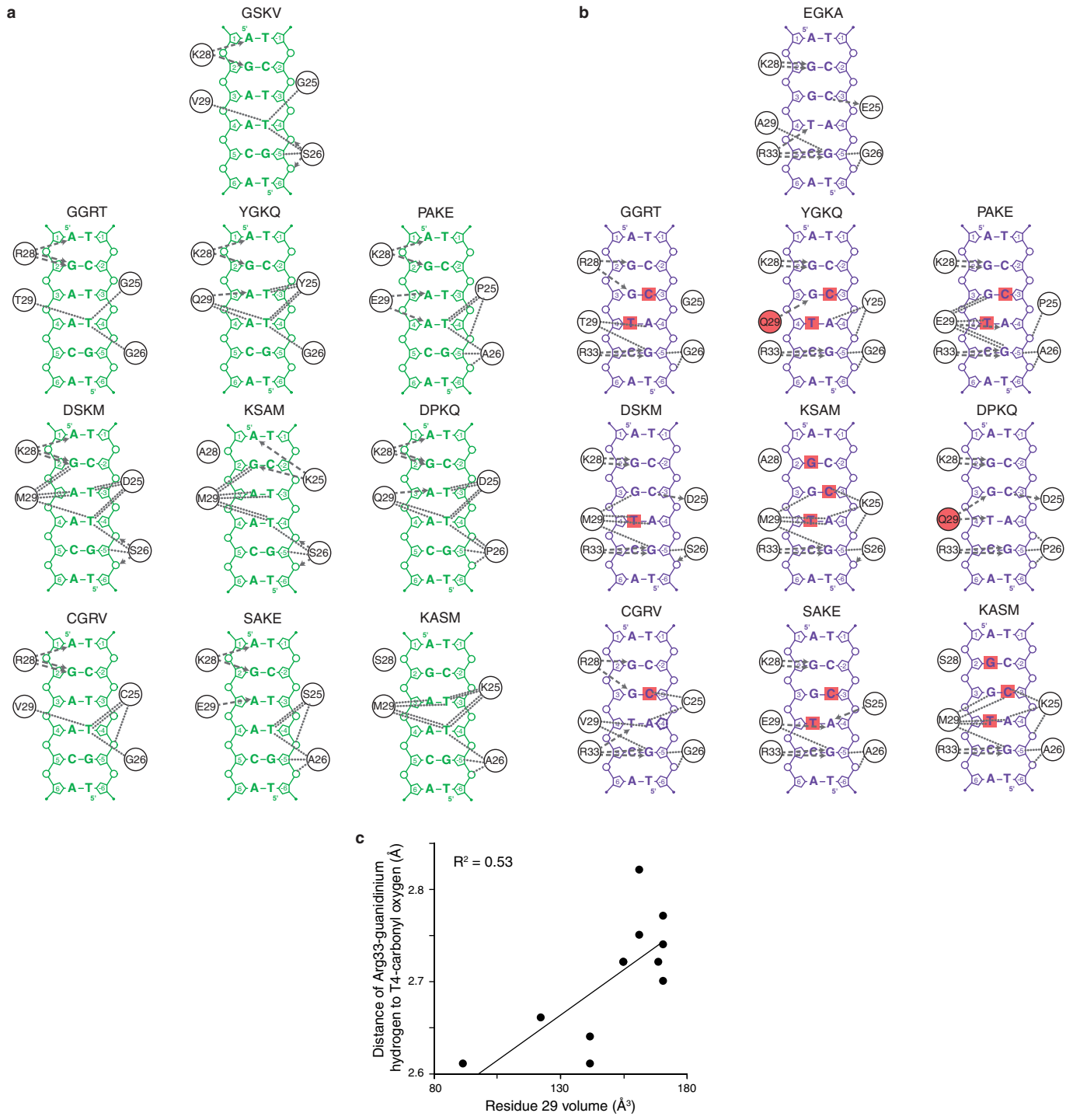

Extended Data Figure 4 | Biophysical diversity in DNA recognition. **a**, **b**, Diverse mechanisms for recognition of SRE (**a**) or ERE (**b**) by the historical RH genotypes (GSKV and EGKA) and alternative SRE-specific variants. Contacts from FoldX-generated structural models are shown between RH residues (circles) and DNA bases (letters), backbone phosphates (small circles) and sugars (pentagons, numbered by position in the DNA motif; dashed numbers refer to the complementary strand). Hydrogen bonds are shown as dashed arrows from donor to acceptor; dotted lines, non-bonded contacts. Red squares, bases that form hydrogen bonds in the EGKA-ERE structure that are unsatisfied in complex with an SRE-specific RH; red circles, side chains with polar groups that are not satisfied in complex with ERE. Only DNA contacts that vary among the analysed structures are shown. **c**, Large side chains at position 29 correlate with the loss of a conserved R33 hydrogen bond to ERE. For ERE-bound structural models, the distance of the Arg33 guanidinium hydrogen to the ERE T4 carbonyl oxygen was measured and compared with the atomic volume of the residue at position 29 in that variant.

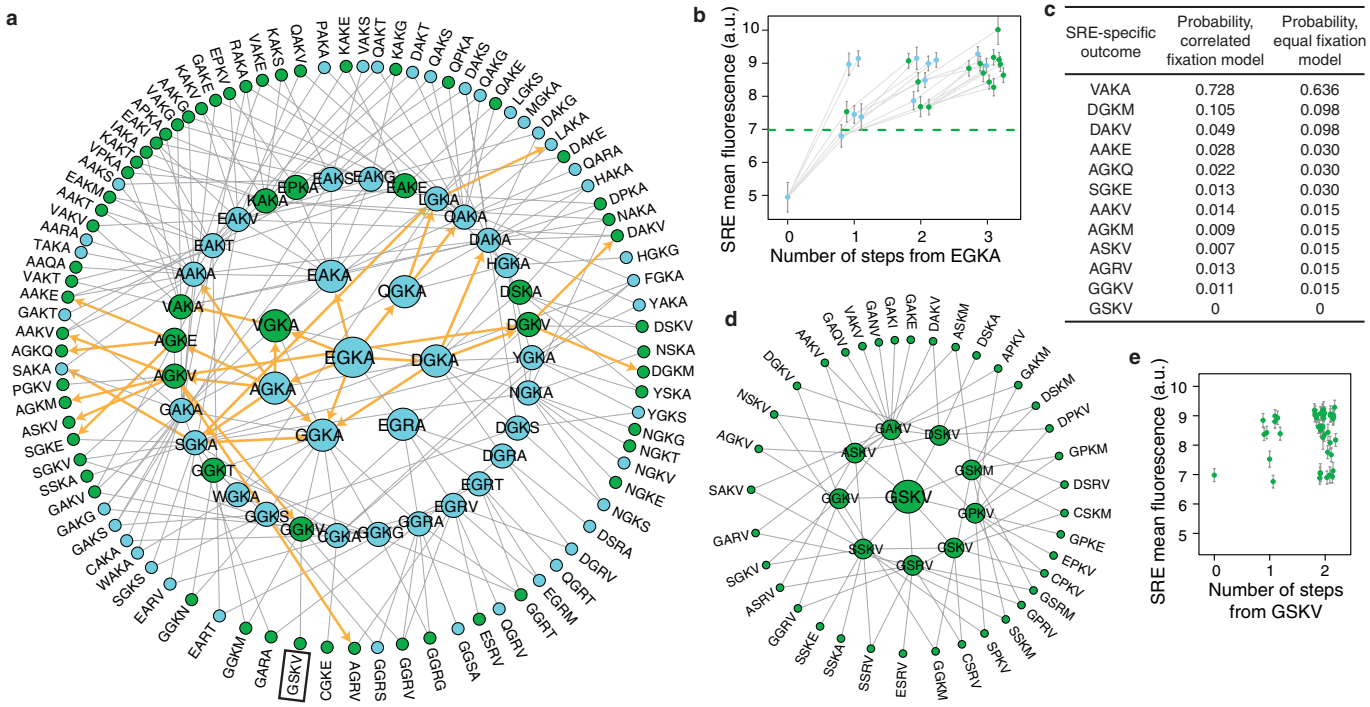

SRE-specific outcome	Probability, correlated fixation model	Probability, equal fixation model
VAKA	0.728	0.636
DGKM	0.105	0.098
DAKV	0.049	0.098
AAKE	0.028	0.030
AGKQ	0.022	0.030
SGKE	0.013	0.030
AAKV	0.014	0.015
AGKM	0.009	0.015
ASKV	0.007	0.015
AGRV	0.013	0.015
GGKV	0.011	0.015
GSKV	0	0

Extended Data Figure 5 | The ancestral RH (EGKA) and derived RH (GSKV) can access many SRE-specific outcomes by short paths in AncSR1+11P. a, Concentric rings contain RH genotypes of minimum path length one, two, or three steps from AncSR1+11P:EGKA (centre). The historical outcome (GSKV, boxed, bottom) is accessible through a three-step path (EGKA–GGKA–GGKV–GSKV). Alternative SRE-specific outcomes accessible in three or fewer steps are in green. Lines connect genotypes separated by a single non-synonymous nucleotide mutation; lines among genotypes in the outer ring are not shown for clarity. Orange arrows indicate paths of significantly increasing SRE mean fluorescence. **b**, For trajectories indicated by orange arrows in **a**, SRE mean fluorescence is shown versus mutational distance from AncSR1+11P:EGKA (with *x*-axis jitter to avoid overplotting). Grey lines connect variants separated by single-nucleotide mutations. Error bars, 90% confidence intervals. Green dashed line, activity of AncSR1+11P:GSKV on SRE. **c**, For the SRE-specific outcomes accessed in orange paths in **a**, the probability of each outcome under models where the probability of taking a step depends on the relative increase in SRE mean fluorescence (correlated fixation model), or where any SRE-enhancing step is equally likely (equal fixation model)[8]. **d**, The historical outcome (GSKV) has SRE-specific single-mutant neighbours. Concentric rings contain SRE-specific RH genotypes of path length one or two steps from AncSR1+11P:GSKV (centre). Lines connect genotypes separated by a single non-synonymous nucleotide mutation; lines among genotypes in the outer ring are not shown for clarity. **e**, The distribution of SRE mean fluorescence of SRE-specific neighbours of AncSR1+11P:GSKV illustrated in **d**. Error bars, 90% confidence intervals.

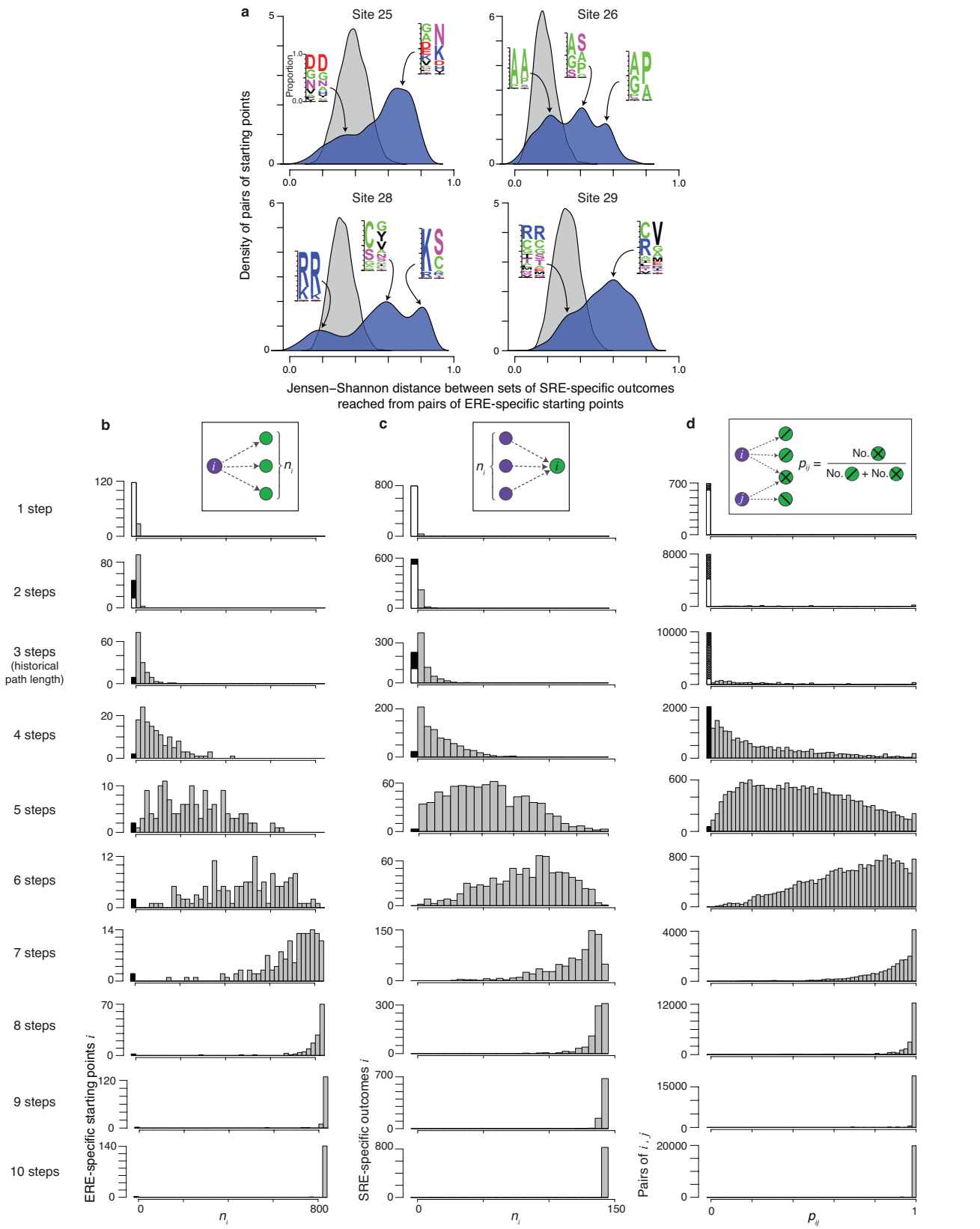

Extended Data Figure 6 | Evolvability of SRE specificity in an ancestral sequence space. a, Alternative ERE-specific starting points reach SRE-specific outcomes with very different amino-acid states. For each starting point accessing at least 15 outcomes (the median of all starting points), the frequency profile of amino-acid states at each RH site was determined for the set of SRE-specific outcomes reached in three or fewer steps; for each pair of starting points, the Jensen–Shannon (J–S) distance between profiles was calculated. Blue curve, distribution of pairs of starting points by J–S distances of the outcomes they reach; grey, distribution of J–S distances between profiles for randomly sampled sets of SRE-specific variants. In each modal peak, the amino-acid frequency profiles for outcomes reached by a representative pair of ERE-specific starting points are shown. **b–d**, Contingency in the accessibility of individual SRE-specific outcomes remains when path lengths longer than the historical trajectory are considered. Plots are equivalent to Fig. 2b–d but for trajectories of increasing length.

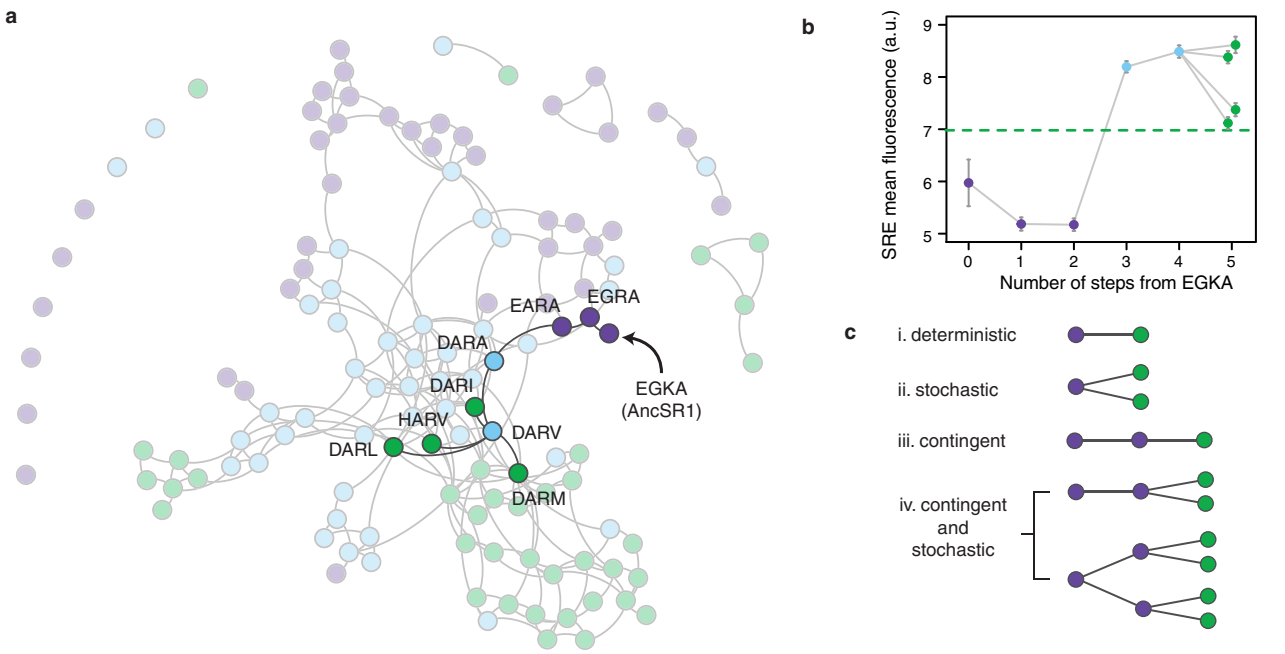

Extended Data Figure 7 | The historical starting point cannot access the derived function without permissive mutations. a, AncSR1 RH functional network layout as in Fig. 3c, with the shortest paths from AncSR1:EGKA to SRE specificity highlighted. The ancestral RH (EGKA) can access SRE specificity. However, all trajectories are at least five steps long, require permissive RH changes that confer no SRE activity (for example, K28R and G26A), and proceed through promiscuous intermediates. **b**, For paths highlighted in **a**, SRE mean fluorescence is shown versus mutational distance from AncSR1:EGKA; grey lines connect variants separated by single-nucleotide mutations. Error bars, 90% confidence intervals. Green dashed line, activity of AncSR1+11P:GSKV on SRE. AncSR1:EGKA was represented by only seven cells in the SRE library, so its FACS-seq SRE mean fluorescence estimate is unreliable (and its classification was thus inferred by the predictive model). In isolated flow cytometry experiments, its SRE mean fluorescence was indistinguishable from null alleles; the decrease in SRE mean fluorescence from step 0 to step 1 suggested by this figure is therefore more probably a flat line (no change in SRE activity). **c**, Stochasticity and contingency in trajectories of functional change. Diagrams illustrate paths from a purple starting point (left) to possible green outcomes (right). In a deterministic trajectory (i), a particular genotype encoding the green function will evolve deterministically if selection favours acquisition of the green function and only that genotype is accessible. The outcome of evolution is stochastic (ii) if multiple outcomes are accessible, so which one occurs is random. An outcome is contingent (iii) if its accessibility depends on the prior occurrence of some step that cannot be driven by selection for that outcome. Contingency and stochasticity can occur independently (ii and iii), or they can co-occur in serial (iv).

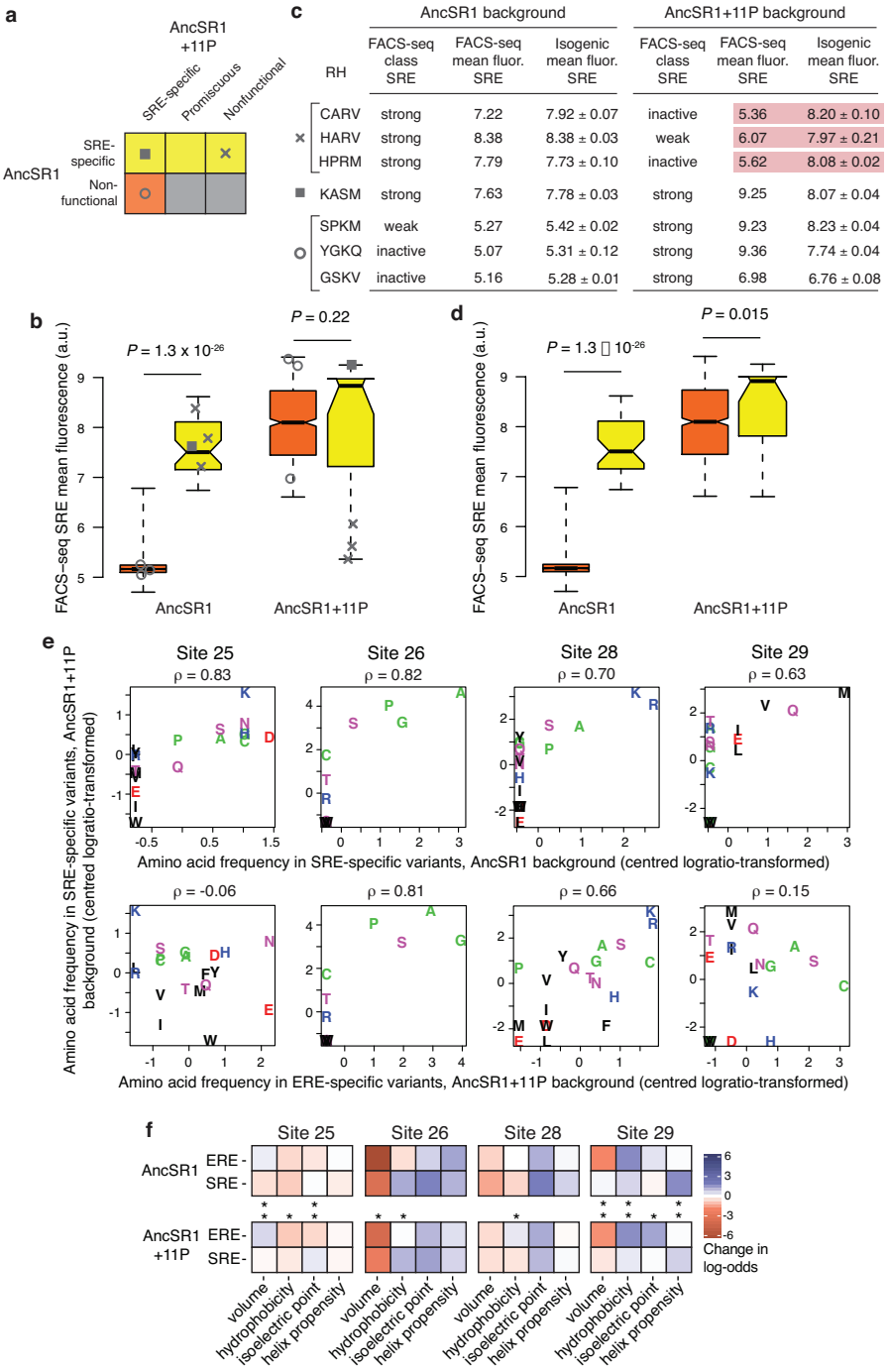

Extended Data Figure 8 | See next page for caption.

Extended Data Figure 8 | The effect of historical permissive substitutions is mediated by non-specific increases in affinity. **a**–**d**, The 11P substitutions non-specifically increase transcriptional activity as measured by FACS-seq, consistent with FoldX predictions of effects on binding affinity. **a**, Classification of SRE-specific variants as 11P-dependent (orange) and 11P-independent (yellow) on the basis of their functions in AncSR1 and AncSR1+11P backgrounds. Icons for individual variants specifically assessed in **b** and **c** are shown. **b**, FACS-seq mean fluorescence estimates for 11P-dependent (orange) and 11P-independent (yellow) RH variants in the AncSR1 (left) and AncSR1+11P (right) backgrounds, shown as box-and-whisker plots as in Fig. 4a. Icons represent variants validated in **c**. *P* values, Wilcoxon rank-sum test with continuity correction. The mean fluorescence of 11P-independent genotypes is significantly higher in the AncSR1 background but not in AncSR+11P. **c**, Validation of apparently restrictive effect of 11P on some genotypes. For three variants non-functional in AncSR1+11P but SRE-specific in AncSR1 FACS-seq assays (×), we measured mean fluorescence of isogenic cultures by flow cytometry. We also assayed variants SRE-specific in AncSR1+11P and SRE-specific (square) or non-functional (open circle) in AncSR1, as validation controls. Isogenic mean fluorescence is represented as mean ± s.e.m. from three replicate transformations and inductions analysed via flow cytometry. All FACS-seq classifications were validated except for the three apparently restricted variants in AncSR1+11P (highlighted in red), which are in fact strong SRE-activators in this background. Each of these variants was predicted to be a strong SRE-binder on the basis of its genotype, but had an artificially low FACS-seq mean fluorescence estimate, perhaps because of a strong growth defect in inducing conditions. **d**, After removing the three genotypes with inaccurate FACS-seq fluorescence measurements (×), 11P-independent genotypes have significantly higher mean fluorescence than 11P-dependent genotypes in the AncSR1+11P background, consistent with a non-specific permissive mechanism via affinity. *P* values, Wilcoxon rank-sum test with continuity correction. **e**, The 11P substitutions do not alter the genetic determinants of SRE specificity. Each plot shows, for a variable site in the library, the frequency of every amino-acid state in two functionally defined sets of variants. Spearman's ρ for each correlation is shown. The top row shows that the determinants of SRE specificity are similar in AncSR1 and AncSR1+11P libraries; the bottom row shows a much weaker relationship between the determinants of SRE and ERE specificity within the AncSR1+11P library. **f**, Biochemical determinants of ERE and SRE specificity in the AncSR1 (top) and AncSR1+11P (bottom) backgrounds. A multiple logistic regression model predicts the probability that a variant is response-element-specific from the biochemical properties of its amino-acid state at each of the four variable RH sites. The coefficients of this model represent the change in log-odds of being ERE-specific or SRE-specific per unit change in each property. Asterisks indicate site-specific determinants that differ significantly between ERE and SRE specificity in each background (Z test, $P < 0.05$).

Extended Data Table 1 | Library sampling statistics

					FACS					sequencing					coverage, all variants		coverage, coding variants	
		bacterial transformation yield (cfu)	yeast transformation yield (cfu)	smallest bottleneck during FACS induction (cfu)	bin 1 count (cfu)	bin 2 count (cfu)	bin 3 count (cfu)	bin 4 count (cfu)	total number cells recovered post-sort (cfu)	bin 1 read count	bin 2 read count	bin 3 read count	bin 4 read count	read:cfu > 1 for all bins?	median number of cells sampled	fraction variants with >15 cells	median number of cells sampled	fraction variants with >15 cells
AncSR1 +11P +RH lib	ERE, rep1	2.32e7	6.12e6	3.2e8	2.02e7	3.38e7	3.22e6	4.74e5	5.77e7	2.75e7	3.64e7	3.32e6	2.01e7	yes	55.4	0.780	61.1	0.797
	ERE, rep 2		1.07e7	4.4e8	1.69e7	1.59e7	2.89e6	1.08e5	3.58e7	3.51e7	3.65e7	7.91e6	1.71e6	yes	64.0	0.830	70.5	0.843
	ERE, pooled		1.68e7	*Not applicable*					9.35e7	*Not applicable*					127.07	0.913	140.3	0.921
	SRE, rep 1		7.10e6	1.0e8	1.58e7	1.31e7	1.79e6	1.86e5	3.09e7	3.02e7	1.57e7	2.58e6	1.13e6	yes	70.7	0.811	78.2	0.826
	SRE, rep 2		1.83e7	2.0e8	2.02e7	3.17e7	4.91e6	4.11e5	5.72e7	2.31e7	6.03e7	1.12e7	3.80e6	yes	64.7	0.836	71.9	0.851
	SRE, pooled		2.54e7	*Not applicable*					8.81e7	*Not applicable*					143.6	0.924	158.9	0.931
AncSR1 +RH lib	ERE, rep1	2.26e7	8.31e6	3.4e8	2.04e7	3.18e7	5.25e6	2.19e5	5.77e7	2.40e7	5.11e7	6.44e6	5.47e5	yes	57.5	0.812	61.3	0.822
	ERE, rep 2		8.63e6	2.6e8	1.58e7	1.61e7	2.82e6	1.56e5	3.49e7	2.50e7	2.85e7	3.54e6	1.12e6	yes	37.1	0.734	39.6	0.748
	ERE, pooled		1.69e7	*Not applicable*					9.26e7	*Not applicable*					104.5	0.907	111.7	0.912
	SRE, rep 1		2.04e7	2.5e8	2.10e7	3.57e7	5.40e6	1.33e5	6.22e7	3.26e7	9.27e7	6.57e6	4.32e5	yes	178.4	0.958	191.3	0.961
	SRE, rep 2		2.06e7	2.9e8	2.03e7	3.07e7	5.54e6	5.86e5	5.71e7	3.14e7	5.53e7	2.01e7	1.55e6	yes	82.7	0.873	89.1	0.881
	SRE, pooled		4.10e7	*Not applicable*					1.19e8	*Not applicable*					289.8	0.979	312.1	0.980

Sample sizes and sequence read/coverage statistics are shown at various stages of the experimental pipeline for each protein library, yeast reporter strain, and replicate. For details, see Methods.

Extended Data Table 2 | Robustness of inferences to scheme for classification of variants

	Classification Scheme										
Inference	Main text	(A) Use FACS-seq ML estimate for AncSR1/ERE	(B) Increase equivalence margin from 20% to 50%	(C) Classify as functional if weak or strong activity	(D) Classify as functional if ML fluorescence >0.8× that of ancestral reference	(E) Classify as functional only if ML fluor within 20% on either side of ancestral reference	(F) Classify all variants based on predictions from genotype	(G) No predictions; classify undetermined variants as inactive	(H) Classify based on prediction or experiment, whichever assigns stronger function	(I) Keep only classifications identical between replicates	(J) Use per-variant estimate of standard error to classify
# ERE-specific, AncSR1	43	138	108	444	67	36	27	39	47	11	47
# promiscuous, AncSR1	45	94	84	158	58	38	45	44	60	30	46
# SRE-specific, AncSR1	41	41	58	213	45	19	31	38	40	39	40
# ERE-specific, AncSR1+11P	144	326	264	619	212	114	101	108	133	76	123
# promiscuous, AncSR1+11P	378	525	554	719	464	254	319	341	459	282	358
# SRE-specific, AncSR1+11P	829	832	1206	2728	956	296	670	768	899	809	837
AncSR1:EGKA requires permissives to access SRE-specificity?	TRUE	TRUE	TRUE	TRUE	TRUE	TRUE	TRUE	TRUE	TRUE	TRUE	TRUE
Shortest path length from EGKA to SRE-specificity in AncSR1	5	5	3	2	5	6	5	5	5	no paths	4
# SRE-specific outcomes accessed in 3 steps from AncSR1+11P:EGKA	65	66	89	136	77	10	58	53	72	71	65
Proportion ERE-specific starting points unable to access SRE-specificity in 3 steps, AncSR1+11P	0.063	0.037	0.008	0.066	0.014	0.252	0.050	0.139	0.053	0.026	0.089
Proportion SRE-specific outcomes not accessed from any ERE-specific starting point in 3 steps, AncSR1+11P	0.276	0.108	0.118	0.071	0.150	0.571	0.378	0.388	0.276	0.425	0.280
Proportion pairs of ERE-specific starting points with no shared outcomes in 3 steps, AncSR1+11P	0.542	0.530	0.426	0.229	0.501	0.836	0.543	0.611	0.529	0.390	0.541
Fraction ERE-specific variants with no path to SRE-specificity, AncSR1	0.279	0.058	0.505	0.054	0.176	0.378	0.321	0.350	0.250	0.083	0.104
Fraction ERE-specific variants with no path to SRE-specificity, AncSR1+11P	0.014	0.021	0.004	0.066	0.005	0.470	0.010	0.056	0.015	0	0.033
Average shortest path length to SRE-specificity from all connected ERE-specific variants, AncSR1	4.193	4.191	3.796	2.309	4.054	4.304	4.158	4.889	4.278	4.545	4.163
Average shortest path length to SRE-specificity from all connected ERE-specific variants, AncSR1+11P	2.183	2.122	1.867	1.336	1.986	2.885	2.270	2.333	2.206	2.158	2.294
Fraction ERE-specific variants with permissive shortest path, AncSR1	0	0.035	0.059	0.242	0	0	0	0	0	0	0
Fraction ERE-specific variants with permissive shortest path, AncSR1+11P	0.290	0.218	0.225	0.191	0.235	0.136	0.207	0.234	0.210	0.140	0.214
Fraction ERE-specific variants with promiscuous shortest path, AncSR1	0.483	0.461	0.381	0.370	0.381	0.445	0.548	0.361	0.594	0.634	0.524
Fraction ERE-specific variants with promiscuous shortest path, AncSR1+11P	0.413	0.462	0.403	0.133	0.441	0.458	0.504	0.426	0.538	0.524	0.475
Fraction ERE-specific variants with permissive and promiscuous shortest path, AncSR1	0.517	0.481	0.530	0.191	0.619	0.555	0.452	0.639	0.406	0.366	0.476
Fraction ERE-specific variants with permissive and promiscuous shortest path, AncSR1+11P	0.108	0.120	0.065	0.002	0.082	0.241	0.149	0.164	0.106	0.165	0.135
Fraction ERE-specific variants with direct shortest path AncSR1	0	0.023	0.030	0.198	0	0	0	0	0	0	0
Fraction ERE-specific variants direct shortest path, AncSR1+11P	0.190	0.201	0.308	0.673	0.242	0.165	0.14	0.176	0.145	0.171	0.176

Each row represents an inference reported in Figs 2 and 3; each column is a scheme for functionally classifying variants from FACS-seq data and FACS-seq-trained predictive models. For details of schemes, see Methods.

nature research

Corresponding Author: Joseph Thornton

Date: Jul 18, 2017

Life Sciences Reporting Summary

Nature Research wishes to improve the reproducibility of the work we publish. This form is published with all life science papers and is intended to promote consistency and transparency in reporting. All life sciences submissions use this form; while some list items might not apply to an individual manuscript, all fields must be completed for clarity.

For further information on the points included in this form, see Reporting Life Sciences Research. For further information on Nature Research policies, including our data availability policy, see Authors & Referees and the Editorial Policy Checklist.

Experimental design

1. Sample size

   Describe how sample size was determined. n/a

2. Data exclusions

   Describe any data exclusions. For FACS-seq, variants with fewer than 15 cells sampled were excluded (lines 552-558); for points excluded in Extended Data Fig. 8d, criteria described in Methods (lines 577-590).

3. Replication

   Describe whether the experimental findings were reliably reproduced. Yes, all FACS-seq experiments were replicated, with reproducibility illustrated in Extended Data Fig. 1d

4. Randomization

   Describe how samples/organisms/participants were allocated into experimental groups. n/a

5. Blinding

   Describe whether the investigators were blinded to group allocation during data collection and/or analysis. n/a

   Note: all studies involving animals and/or human research participants must disclose whether blinding and randomization were used.

6. Statistical parameters

   For all figures and tables that use statistical methods, confirm that the following items are present in relevant figure legends (or the Methods section if additional space is needed).

n/a	Confirmed	
☐	☒	The exact sample size (*n*) for each experimental group/condition, given as a discrete number and unit of measurement (animals, litters, cultures, etc.)
☐	☒	A description of how samples were collected, noting whether measurements were taken from distinct samples or whether the same sample was measured repeatedly.
☐	☒	A statement indicating how many times each experiment was replicated
☐	☒	The statistical test(s) used and whether they are one- or two-sided (note: only common tests should be described solely by name; more complex techniques should be described in the Methods section)
☐	☒	A description of any assumptions or corrections, such as an adjustment for multiple comparisons
☐	☒	The test results (e.g. *p* values) given as exact values whenever possible and with confidence intervals noted
☐	☒	A summary of the descriptive statistics, including central tendency (e.g. median, mean) and variation (e.g. standard deviation, interquartile range)
☐	☒	Clearly defined error bars

See the web collection on statistics for biologists for further resources and guidance.

Software

Policy information about availability of computer code

7. Software

Describe the software used to analyze the data in this study.	All analysis was performed using custom scripts in R, which are included as Supplementary Information and at the included github link. All additional packages used are described and cited in the Methods.

For all studies, we encourage code deposition in a community repository (e.g. GitHub). Authors must make computer code available to editors and reviewers upon request. The *Nature Methods* guidance for providing algorithms and software for publication may be useful for any submission.

Materials and reagents

Policy information about availability of materials

8. Materials availability

Indicate whether there are restrictions on availability of unique materials or if these materials are only available for distribution by a for-profit company.	All unique materials are readily available from the authors

9. Antibodies

Describe the antibodies used and how they were validated for use in the system under study (i.e. assay and species).	n/a

10. Eukaryotic cell lines

a. State the source of each eukaryotic cell line used.	The yeast strain used was described in Fox et al. (ref. 31)
b. Describe the method of cell line authentication used.	n/a
c. Report whether the cell lines were tested for mycoplasma contamination.	n/a
d. If any of the cell lines used in the paper are listed in the database of commonly misidentified cell lines maintained by ICLAC, provide a scientific rationale for their use.	n/a

Animals and human research participants

Policy information about studies involving animals; when reporting animal research, follow the ARRIVE guidelines

11. Description of research animals

Provide details on animals and/or animal-derived materials used in the study.	n/a

Policy information about studies involving human research participants

12. Description of human research participants

Describe the covariate-relevant population characteristics of the human research participants.	n/a

Corresponding Author: Joseph Thornton

Date: Jul 18, 2017

Flow Cytometry Reporting Summary

Form fields will expand as needed. Please do not leave fields blank.

Data presentation

For all flow cytometry data, confirm that:

☒ 1. The axis labels state the marker and fluorochrome used (e.g. CD4-FITC).

☒ 2. The axis scales are clearly visible. Include numbers along axes only for bottom left plot of group (a 'group' is an analysis of identical markers).

☒ 3. All plots are contour plots with outliers or pseudocolor plots.

☒ 4. A numerical value for number of cells or percentage (with statistics) is provided.

Methodological details

5. Describe the sample preparation.	Methods lines 395-443
6. Identify the instrument used for data collection.	BD FACSAria II (Methods line 444)
7. Describe the software used to collect and analyze the flow cytometry data.	Gates drawn using BD FACSDIVA software; all further analyses were performed in R (scripts included)
8. Describe the abundance of the relevant cell populations within post-sort fractions.	Recovery yield from post-sort fractions was estimated by plating dilutions of cells and counting colony forming units
9. Describe the gating strategy used.	Methods lines 444-450, Extended Data Fig. 2

Tick this box to confirm that a figure exemplifying the gating strategy is provided in the Supplementary Information. ☒